Monthly Notices of the ROYAL ASTRONOMICAL SOCIETY

MNRAS **541,** 3081–3100 (2025) https://doi.org/10.1093/mnras/staf1159
Advance Access publication 2025 July 25

# WISDOM Project – XXIV. Giant molecular clouds of the spiral galaxy NGC 5064: high fraction of retrograde rotation

Lijie Liu [1,2,3★] Fanglin Shu [4] Martin Bureau,[5,6] Kyoko Onishi,[7] Timothy A. Davis [8] Fu-Heng Liang [5] Woorak Choi [9] Thomas G. Williams [5] Anan Lu [10] and Satoru Iguchi [11,12]

[1]*Cosmic Dawn Center (DAWN), Copenhagen, Denmark*
[2]*Niels Bohr Institute, University of Copenhagen, Lyngbyvej 2, 2100 Copenhagen Ø, Denmark*
[3]*DTU-Space, Technical University of Denmark, Elektrovej 327, DK2800 Kgs. Lyngby, Denmark*
[4]*Wadham College, University of Oxford, Parks Road, Oxford OX1 3PN, UK*
[5]*Sub-department of Astrophysics, Department of Physics, University of Oxford, Keble Road, Oxford OX1 3RH, UK*
[6]*Yonsei Frontier Lab and Department of Astronomy, Yonsei University, 50 Yonsei-ro, Seodaemun-gu, Seoul 03722, Republic of Korea*
[7]*Department of Space, Earth and Environment, Chalmers University of Technology, Onsala Observatory, SE-439 92 Onsala, Sweden*
[8]*Cardiff Hub for Astrophysics Research & Technology, School of Physics & Astronomy, Cardiff University, Queens Buildings, Cardiff CF24 3AA, UK*
[9]*Department of Astronomy, Yonsei University, 50 Yonsei-ro, Seodaemun-gu, Seoul 03722, Republic of Korea*
[10]*Trottier Space Institute and Department of Physics, McGill University, 3600 University Street, Montreal QC H3A 2T8, Canada*
[11]*Department of Astronomical Science, SOKENDAI (The Graduate University of Advanced Studies), Mitaka, Tokyo 181-8588, Japan*
[12]*National Astronomical Observatory of Japan, Mitaka, Tokyo 181-8588, Japan*

Accepted 2025 July 7. Received 2025 July 1; in original form 2023 November 9

## ABSTRACT

We present high-resolution (0.14 arcsec × 0.12 arcsec or $31 \times 25\,\mathrm{pc}^2$) Atacama Large Millimeter/sub-millimeter Array $^{12}$CO($J = 2$–1) observations of the spiral galaxy NGC 5064. Our study identifies 478 molecular clouds, of which 387 are resolved both spatially and spectrally. These clouds exhibit similarities to those of the Milky Way in terms of their sizes, molecular gas masses, velocity dispersions, velocity gradients, and Larson relations. However, the NGC 5064 clouds stand out with slightly higher gas mass surface densities, lower virial parameters ($\langle\alpha_{\rm vir}\rangle = 0.48 \pm 0.03$ assuming a standard conversion factor $X_{\rm CO} = 2 \times 10^{20}\,\mathrm{cm^{-2}}\,(\mathrm{K\,km\,s^{-1}})^{-1}$; $\alpha_{\rm vir} = 1$ for a lower conversion factor of $X_{\rm CO} = 0.96 \pm 0.02 \times 10^{20}\,\mathrm{cm^{-2}}\,(\mathrm{K\,km\,s^{-1}})^{-1}$), and an unusually high fraction of retrograde rotation ($f_{\rm retro} \approx 67$ per cent). Retrograde clouds are 18 per cent larger, 58 per cent more massive, 15 per cent more turbulent and have 17 per cent larger gas mass surface densities than prograde clouds. The velocity gradients in the clouds seem to arise from turbulence rather than cloud's intrinsic rotation or large-scale galaxy rotation. Cloud–cloud collisions provide the most plausible explanation for the elevated retrograde fraction, though further investigation is needed to confirm this scenario. Projection effects due to the galaxy's high inclination ($i = 70.^{\circ}8$) may further enhance the apparent retrograde fraction. Confirmation using less inclined systems is essential to determine whether the observed dominance of retrograde rotation reflects a genuine physical phenomenon or is significantly shaped by projection effects.

**Key words:** ISM: clouds – galaxies:individual: NGC 5064 – galaxies: ISM – galaxies: nuclei – galaxies: spiral – radio lines: ISM.

## 1 INTRODUCTION

Giant molecular clouds (GMCs) are the densest part of the interstellar medium and are responsible for most star formation (see e.g. Fukui & Kawamura 2010 for a review). Understanding the physical properties of GMCs is therefore crucial to understand star-formation processes. Early studies of the Milky Way and late-type disc galaxies in the Local Group revealed that their GMCs have similar physical properties. The clouds of these galaxies follow similar Larson relations (e.g. size–linewidth relation; Solomon et al. 1987) and are in approximate virial equilibria (e.g. Blitz et al. 2007; Bolatto et al. 2008; Hirota et al. 2011; Wong et al. 2011). However, clouds in the Galactic Centre (e.g. Miyazaki & Tsuboi 2000; Oka et al. 2001; Rice et al. 2016; Kauffmann et al. 2017) and other galaxy centres (e.g. NGC 4826, Rosolowsky & Blitz 2005; NGC 6946, Donovan Meyer et al. 2013; NGC 4429, Liu et al. 2021; NGC 404, Liu et al. 2022; NGC 5806 and Choi et al. 2023) appear to depart from the usual Larson relations and often have higher velocity dispersions at a given size. The first study of GMCs in an early-type galaxy (NGC 4526, Utomo et al. 2015) showed no size–linewidth relation. Recent observations also show that many GMCs in some galaxies are only marginally gravitationally bound (e.g. NGC 4429, Liu et al. 2021) or are predominantly gravitationally unbound (or pressure confined; e.g. M 51, Colombo et al. 2014; NGC 4526, Utomo et al. 2015; inner Galaxy, Miville-Deschenes, Murray & Lee 2017a; NGC 6826,

★ E-mail: ljliu.astro@gmail.com

Schruba et al. 2017). It is thus essential to study the similarities and differences of cloud properties in a variety of galactic environments.

The internal kinematics of GMCs can provide insights into their dynamical states and surrounding environments (e.g. Goldreich & Sridhar 1995). Recent studies revealed small velocity gradients (0.03–0.05 km s$^{-1}$ pc$^{-1}$) in the clouds of the flocculent, late-type spiral galaxies M 33 (Braine et al. 2018) and M 51 (Braine et al. 2020). If these observed velocity gradients arise from internal cloud rotation, the rotational energies of the GMCs in M 33 and M 51 are only 1–2 per cent of their self-gravitational energies (Braine et al. 2018, 2020), suggesting that cloud rotation contributes very little to cloud support against self-gravity in these late-type spirals. On the other hand, significant velocity gradients (0.05–0.09 km s$^{-1}$ pc$^{-1}$) are present in the clouds of the early-type galaxies NGC 4526 (Utomo et al. 2015) and NGC 4429 (Liu et al. 2021), where the rotational energies of the GMCs can be as important as their self-gravitational energies (Liu et al. 2021). The degree of cloud rotation (often parametrized by the ratio of a cloud's rotational energy to its self-gravitational energy) has important implications for star formation; slow-rotating clouds are more likely to form high-mass stars and fast-rotating clouds low-mass stars (Raghuvanshi & Dutta 2022).

It remains unclear what drives the observed velocity gradients of clouds. Due to resolution and sensitivity limitations, spatially resolved studies of cloud kinematics in external galaxies are still relatively new and few. Simulations suggest that turbulence can produce observed linear velocity gradients that can easily be interpreted as solid-body cloud rotation (Burkert & Bodenheimer 2000; Misugi, Inutsuka & Arzoumanian 2019). Braine et al. (2018, 2020), however, claimed that the velocity gradients observed in the clouds of M 33 and M 51 are not due to random dynamical forces such as turbulence, but have been inherited from the rotating galactic disc out of which they formed. Utomo et al. (2015) and Liu et al. (2021) showed that the velocity gradients of the clouds in the early-type galaxies NGC 4526 and NGC 4429 arise primarily from the projection of the large-scale galaxy rotation on cloud scale.

It is thus of interest to probe how molecular clouds rotate with respect to the large-scale rotation of their host galaxy. In this paper, we will thus use the terms prograde and retrograde to indicate whether the internal rotation (and thus angular momentum) of a cloud is aligned or not with that of the large-scale bulk gas rotation around the galaxy as observed from Earth (and not to indicate whether an individual cloud's path around the galaxy is in the same sense or not as that of the bulk of the stars). In the Milky Way, observations show that the rotation axes of the clouds are randomly oriented, with near-equal fractions of prograde and retrograde clouds (Phillips 1999; Koda et al. 2006; Hernandez & Tan 2015). Similar observations have also been reported in the nearby barred spiral galaxy NGC 5806, as described in a recent study by Choi et al. (2023). Studies of M 33 and M 51, however, show that the clouds are mostly prograde (≈ 70 per cent; Imara, Bigiel & Blitz 2011a; Braine et al. 2018, 2020), although their angular velocities are much smaller than those of the galaxy at local scales. In early-type galaxies (NGC 4526 and NGC 4429), clouds are also mostly prograde, with their projected rotational axes strongly aligned with the isovelocity contours of the large-scale galaxy rotation, and their velocity gradients are comparable to those of the galaxy (Utomo et al. 2015; Liu et al. 2021).

As part of the mm-Wave Interferometric Survey of Dark Object Masses (WISDOM), we investigate in this paper the properties of the clouds in the spiral galaxy NGC 5064. In particular, we probe whether the clouds follow Larson's relations and/or are in virial equilibrium. We also measure the internal bulk motions (velocity gradients and rotational axes) of the clouds and consider their origin.

The structure of this paper is as follows: In Section 2, we present our observations and GMC identification method. The basic properties of the GMCs identified are summarized in Section 3, while we assess the dynamical states of the clouds in Section 4 by discussing Larson's relations and the virial parameter. The kinematics of the clouds is quantified in Section 5, while we discuss in turn the origin of the observed high fraction of retrograde clouds and turbulence, the effects of external gravity on GMC properties and the CO-to-$H_2$ conversion factor in Section 6. We summarize our findings and conclude briefly in Section 7.

## 2 DATA AND CLOUD IDENTIFICATION

### 2.1 Target: NGC 5064

NGC 5064 is a nearby early-type spiral galaxy ((R′)SAab) located at RA = 13$^{\rm h}$18$^{\rm m}$59$^{\rm s}$.9, Dec. = −47°54′31″.15 (J2000.0). We adopt a distance of 45.5 Mpc by taking the median of the five most recent redshift-independent measurements based on the Tully–Fisher (rotation velocity–luminosity; Willick et al. 1997; Tully et al. 2013; Sorce et al. 2014; Tully, Courtois & Sorce 2016) and fundamental plane (Springob et al. 2014) relations, so 1″ corresponds to ≈ 220 pc. Fig. 1 presents an overview of the galaxy. The left panel shows an optical image from the STScI Digitized Sky Survey (DSS; Kent 1994), while the right panel displays the *HST* WFPC2 F606W band image with $^{12}$CO(2–1) intensity contours overlaid. The $^{12}$CO(2–1) data, obtained in this work, are described in Section 2.2. NGC 5064 hosts a low-ionization nuclear emission-line region (Veron-Cetty & Veron 1986; Vaceli et al. 1997), but no other sign of nuclear activity has yet been detected. The kinematics of its H$\alpha$ emission reveals a typical rotation curve, with solid-body rotation extending up to a galactocentric radius $R_{\rm gal} \approx 4''$, followed by an approximately constant rotation velocity $V_{\rm rot} \approx 200$ km s$^{-1}$ (Bertola et al. 1998). The stellar velocity dispersion within one effective radius ($\sigma_{\rm e} \approx 210$ km s$^{-1}$; Vega Beltrán et al. 2001) and the $M_{\rm BH} - \sigma_{\rm e}$ relation of van den Bosch et al. (2016) yield an estimate of the supermassive black hole (SMBH) mass of $2.7 \times 10^8$ M$_\odot$. Our kinematic analysis of the molecular gas disc, conducted using the same data set as in this study, indicates the existence of an SMBH with a mass of $(1.24 \pm 0.78) \times 10^8$ M$_\odot$ (Onishi et al. in prep.). Additionally, the best-fitting parameters include an inclination of 70°.8 and a kinematic position angle of 35° (see Section 5.2 for details).

The total star-formation rate of NGC 5064 has been estimated to be ≈ 1.2 M$_\odot$ yr$^{-1}$ using the total infrared luminosity (8–1000 μm; Davis et al. 2022). The $^{12}$CO ($J = 2 - 1$) total flux obtained with Atacama Pathfinder Experiment (APEX) gives an estimate of a total molecular gas mass, approximately $1.8 \times 10^9$ M$_\odot$ (see Section 2.2 for details on the APEX observations). NGC 5064 thus has a global star-formation efficiency SFE ≡ SFR/$M_{\rm H_2}$ ≈ $6.7 \times 10^{-10}$ yr$^{-1}$, or equivalently a molecular gas depletion time $t_{\rm dep} \equiv {\rm SFE}^{-1} \approx 1.5$ Gyr. This depletion time is close to the typical depletion times of nearby spiral galaxies (≈ 2 Gyr; e.g. Bigiel et al. 2008), suggesting NGC 5064 forms stars with similar efficiency as typical spirals.

### 2.2 Observations

NGC 5064 was observed as part of the WISDOM project, targeting the $^{12}$CO($J$ = 2–1) line (rest frequency ≈ 230 GHz) using the Atacama Large Millimeter/submillimeter Array (ALMA). The observations were conducted with the 12-m array of ALMA (Project code 2015.1.00466.S; PI: K. Onishi) and the 7-m array of the

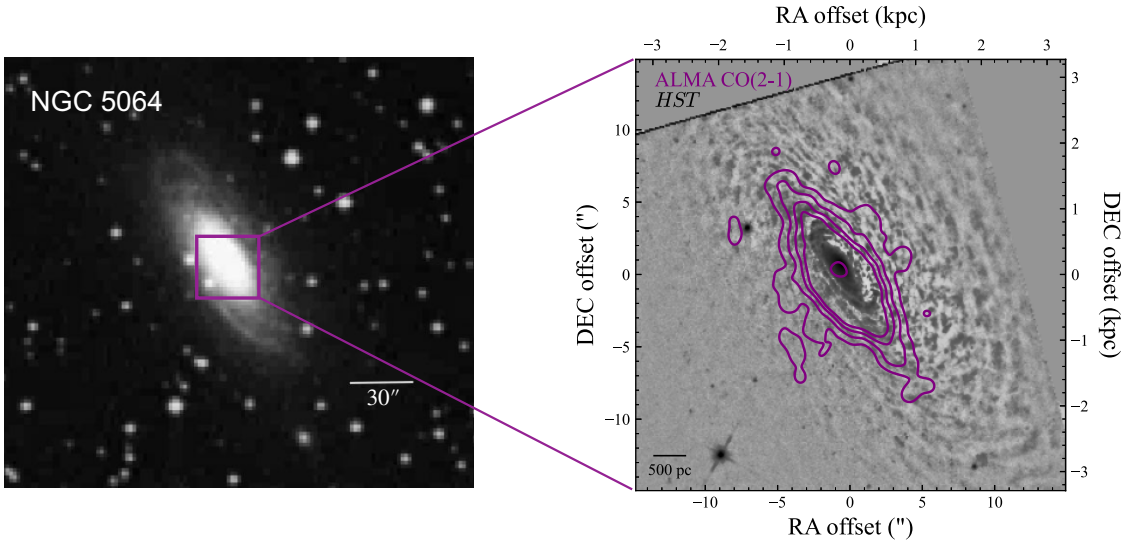


**Figure 1.** The overview images of NGC 5064. *Left:* optical image from the STScI Digitized Sky Survey (DSS; Kent 1994). *Right: HST* WFPC2 F606W image processed with unsharp masking (van der Walt et al. 2014) to emphasize dust features, overlaid with a smoothed ALMA $^{12}$CO(2–1) intensity map shown in purple contours. Scale bars are included in both panels.

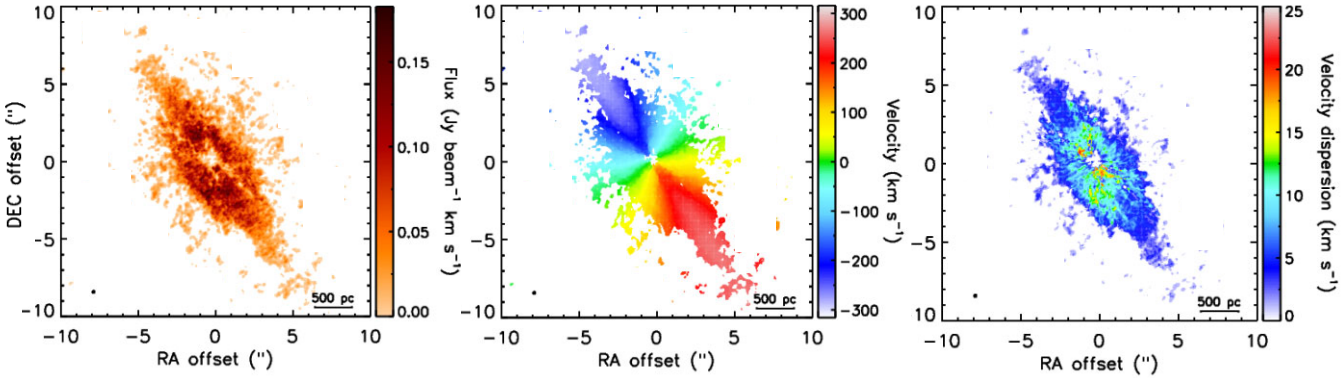


**Figure 2.** $^{12}$CO(2–1) moment maps of NGC 5064. *Left:* zeroth-moment (integrated intensity) map. *Middle:* first-moment (intensity-weighted mean velocity) map. *Right:* second-moment (intensity-weighted velocity dispersion) map. The synthesized beam of 0.14 arcsec × 0.12 arcsec (31 × 25 pc$^2$) is shown in the bottom-left corner of each map as a black solid ellipse.

Atacama Compact Array (Project code 2016.2.00053.S; PI: L. Liu) to ensure optimal $uv$-plane coverage. The observing campaign spanned multiple dates, including 2015 November 20 and 26, and 2016 March 5 and 27, with two different configurations of the 12-m array. Additional observations took place on 2017 June 27 and 28, utilizing the 7-m array. The 12-m array had a total on-source integration time of 29 min, acquired at an hour angle of approximately −4 and −1 h in November and March, respectively. The 7-m array had a total on-source integration time of 19 min at an hour angle of approximately 0 h. The 12-m array consisted of 43 and 42 12-m antennae on November 20th and 26th, respectively, covering baseline lengths of 2–11 053 m, allowing for a maximum recoverable scale of 2.0 arcsec. For the observations on March 5th and 27th, the 12-m array had 38 and 41 antennae, respectively, with baseline lengths of 15–460 m and a maximum recoverable scale of 10.8 arcsec. The 7-m array comprised 9 7-m antennae covering baseline lengths of 9–45 m and a maximum recoverable scale of 29.0 arcsec. This encompasses the full extent of the CO seen in Fig. 2.

The receivers were tuned to cover the frequency range 242.568–246.556 GHz (upper side band, 256 channels) and 227.314–231.186 GHz (lower side band, 3840 channels up to 229.189 GHz, then 128 channels for the rest). The CO($J$ = 2–1) emission line was detected in the lower side band from 227.98 to 228.51 GHz with a raw channel width of 0.488 MHz. For calibration purposes, the 12-m array employed J1427−4206 (bandpass and phase calibrator), J1307−5019 (phase calibrator) and J1107−4449 (flux calibrator). The 7-m array used J1256−0547 (bandpass calibrator), Callisto (flux calibrator), and J1326−5256 (phase calibrator).

We also conducted observations of NGC 5064 using the APEX 12-m single-dish telescope in service mode (PI: T. Davis; proposal O-093.F-9309A), to obtain the integrated spectrum of CO($J$ = 2–1). The total integration time was 18 min, with a mean system temperature of 146 K. The APEX receiver was tuned to cover the frequency range 226.261–230.253 GHz, utilizing 524 channels with a channel separation of 7.63 MHz or ≈ 10 km s$^{-1}$. The $^{12}$CO(2–1) total flux of ≈ 340 Jy km s$^{-1}$, obtained using APEX (beam size of FWHM ≈ 27″), yields a total molecular hydrogen gas mass $M_{\rm H_2} \approx 1.8 \times 10^9$ M$_\odot$ when combined with the standard Galactic conversion factor $X_{\rm CO} = 2 \times 10^{20}$ cm$^{-2}$ (K km s$^{-1}$)$^{-1}$ (Strong & Mattox 1996; Dame, Hartmann & Thaddeus 2001) and a typical

$^{12}$CO(2–1)/$^{12}$CO(1–0) intensity ratio of 0.8 (when expressed in temperature units; Bigiel et al. 2008; Carilli & Walter 2013).

### 2.3 Data

The data were processed using `Common Astronomy Software Applications` (`CASA`; CASA Team et al. 2022) following standard procedures. The two 12-m array configurations, along with the single 7-m array configuration, were first merged to fill the $uv$ plane. Initially, we tried using all the $uv$ components to achieve the best angular resolution, but due to insufficient signal-to-noise ratios to probe the kinematics, we ultimately decided to taper the outer $uv$ components to optimize the sensitivity and angular resolution. We employed a taper with a full-width at half-maximum (FWHM) of 1000 kilolambda ($\approx$ 1314 m) and applied Briggs weighting. The continuum-subtracted dirty cube was cleaned in interactively identified regions of source emission in each channel, to a threshold equal to the root mean square (RMS) noise of the dirty channels. The clean components were then added back and re-convolved using a Gaussian beam of FWHM equal to that of the dirty beam.

The resulting data cube has a synthesized beam of 0.14 arcsec $\times$ 0.12 arcsec (31 $\times$ 25 pc$^2$) at a position angle of 35°. Each (binned) channel has a width of 2 km s$^{-1}$ and the spaxel size is 0.05 arcsec $\times$ 0.05 arcsec ($\approx$ 7 spaxel$^2$ across the synthesized beam). The detected $^{12}$CO(2–1) emission line spans $-$280–280 km s$^{-1}$ with respect to the systemic velocity of NGC 5064 ($\sim$ 2980 km s$^{-1}$, Bertola et al. 1998). The RMS noise in line-free regions of the data cube is $\sigma_{\rm rms}$ = 1.17 mJy beam$^{-1}$ (1.69 K) per (binned) channel. The observations cover a primary beam (field of view) of $\approx 25'' \times 25''$ ($\approx$ 5500 $\times$ 5500 pc$^2$), encompassing the central molecular gas disc of NGC 5064.

Fig. 2 shows the moment maps, including the integrated flux (moment 0), intensity-weighted mean velocity (moment 1) and intensity-weighted velocity dispersion (moment 2) maps. These moment maps were derived from our data cube using a masked-moment technique (Dame 2011). To optimize the moments, we initially created a smoothed cube by applying Hanning smoothing to the original data cube in velocity and spatially smoothing it with a Gaussian kernel matching the FWHM of the synthesized beam. We then generated a mask by selecting only areas of structured emission in the original cube and excludes regions with no significant emission. This process resulted in improved moment maps.

Our ALMA observations reveal a central molecular gas disc with a regular morphology and an outer radius of $\approx$ 1500 pc. We note that the central hole (see Fig. 2) may not be genuine and could fill up with emission with more sensitive data. However, it does indicate the presence of a central CO depression. The CO kinematics shows that the molecular gas is in nearly perfect circular motion with no disturbance, suggesting there is only one kinematic component in the central regions. The molecular gas velocity dispersions within the galaxy increase gradually inward, ranging from $\approx$ 5 km s$^{-1}$ in the outer regions to $\approx$ 20 km s$^{-1}$ in the central regions. The very high-velocity dispersions observed in the very centre of NGC 5064 may be partially attributed to beam smearing effects. The integrated $^{12}$CO(2–1) spectrum of a $9'' \times 9''$ central region of NGC 5064 exhibits the double-horn shape characteristic of a rotating disc (see Fig. 2), with an integrated flux of 181 $\pm$ 10 Jy km s$^{-1}$ (see Fig. 3). Compared to the aforementioned APEX observations with a beam size of FWHM $\approx 27''$, our ALMA observations resolve out $\approx$ 46 per cent of the $^{12}$CO(2–1) flux.

### 2.4 Cloud identification

GMC candidates in NGC 5064 were identified using our modified `CPROPSTOO` algorithm (Liu et al. 2021), an updated version of the widely used `CPROPSTOO` code (Rosolowsky & Leroy 2006; Leroy et al. 2015). Our version is more efficient and robust to identify GMCs, especially in crowded environments. In particular, it (i) captures multiscale cloud structures with less arbitrariness (i.e. fewer free/input parameters) and (ii) decreases the computation time to identify cloud candidates (i.e. local maxima).

The main steps of the algorithm are as follows. First, a spatially varying estimate of the noise is created. This noise cube is then used to construct a mask of significant emission, including only pixels for which both adjacent channels have flux densities $\geq 3\,\sigma_{\rm rms}$. This mask is then expanded to encompass all emission with at least two adjacent channels with flux densities $\geq 2\,\sigma_{\rm rms}$. Regions thus identified are known as 'islands'. To remove noise peaks, only islands with projected areas greater than 10 synthesized beams (or $\approx 93 \times 93$ pc$^2$) are retained. The total flux from these islands is approximately $\approx 105 \pm 15$ Jy km s$^{-1}$, representing about $\sim$ 58 per cent of the integrated flux observed by ALMA. Using a smaller island minimum size only affects the masked emission in the outer regions (galactocentric radii $R_{\rm gal} \gtrsim 900$ pc). We apply the same procedure to an inverted data cube and find no false positives, suggesting the masking criteria are robust.

The code then decomposes the islands identified into individual clouds. Local maxima (i.e. cloud candidates) are identified within running $3 \times 3 \times 3$ pixel$^3$ subsets of the data cube (i.e. 0.15 arcsec $\times$ 0.15 arcsec $\times$ 6 km s$^{-1}$ sub-cubes). To eliminate noise peaks and outliers, the total emission in each $3 \times 3 \times 3$ pixel$^3$ subcube is required to be greater than that in the eight spatially neighbouring subcubes. We then run `CPROPSTOO` by setting the minimum number of channels spanned by a cloud (minvchan = 2) and the minimum contrast between a cloud's peak and its boundary ($\Delta T_{\rm min} = 2\ \sigma_{\rm rms} \approx 3.4$ K). To minimize potential biases introduced by using an either low or high minimum cloud area ($minarea$) and/or minimum number of pixels ($minpix$), we probe a range of $minarea$ and $minpix$ (and set $minarea = minpix$). This thus allows cloud structures of different spatial scales to be identified with a given minimum convexity ($minconvexity$), where $convexity$ is defined as the ratio of the volume of a cloud's 3D intensity distribution to the volume of the smallest convex hull encompassing all of its flux (see Liu et al. 2021). In practice we probe 100 $\leq$ minarea $\leq$ 5 spaxels (and 100 $\leq$ minpix $\leq$ 5 pixels) with a step size of 5 spaxels (and 5 pixels; approximately half the synthesized beam) and adopt mincovexity = 0.4.

Each local maximum that survives the above steps is deemed to be a cloud. Our modified `CPROPSTOO` code applies a 'friends-of-friends' algorithm to assign all emission from 'islands' to each cloud, whereby no assumption about the shape of each cloud is necessary and clouds are guaranteed to be composed of contiguous pixels. A detailed explanation of our modified `CPROPSTOO` code can be found in Liu et al. (2021).

As a result of this analysis, and as shown in Fig. 4, 478 GMCs are identified in NGC 5064, of which 387 are spatially and spectrally resolved, i.e. their deconvolved diameters are larger than the synthesised beam width in two dimensions and their deconvolved velocity widths are wider than half of one (binned) channel.

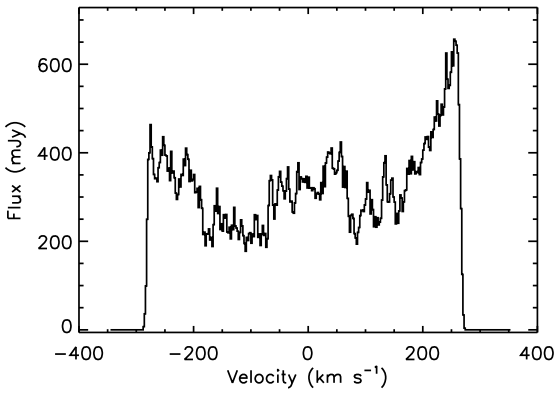


**Figure 3.** Integrated $^{12}$CO(2–1) spectrum of NGC 5064, extracted from a $9'' \times 9''$ region centred on the galaxy centre. The detected $^{12}$CO(2–1) emission line spans $-280$–$280\,\mathrm{km\,s^{-1}}$ with respect to the systemic velocity of NGC 5064 ($\sim 2980$ km s$^{-1}$, Bertola et al. 1998).

## 3 CLOUD PROPERTIES

### 3.1 GMC properties

A number of properties are either directly measured or inferred for each cloud, as described in Rosolowsky & Leroy (2006), Leroy et al. (2015), and Liu et al. (2021). These are listed in Table 1 and include each cloud's position (flux-weighted mean), deprojected distance from the galaxy centre ($R_{\rm gal}$; assuming an infinitely thin disc and the inclination and position angle adopted in Section 5.2), local standard of rest velocity ($V_{\rm LSR}$; flux-weighted mean), size (radius $R_{\rm c}$; deconvolved second spatial moment extrapolated to zero intensity, with scaling factor $\eta = 1.91$ for a constant-density spherical cloud), observed velocity dispersion ($\sigma_{\rm obs,los}$; deconvolved second velocity moment extrapolated to zero intensity), gradient-subtracted velocity dispersion ($\sigma_{\rm gs,los}$; removing internal bulk motions), total $^{12}$CO(2–1) luminosity ($L_{\rm CO(2-1)}$; total flux extrapolated to zero intensity), and total molecular gas mass ($M_{\rm gas}$; including He) derived by adopting a Galactic conversion factor of $2 \times 10^{20}$ cm$^{-2}$ (K km s$^{-1}$)$^{-1}$ (Strong & Mattox 1996; Dame et al. 2001) and a typical $^{12}$CO(2–1)/$^{12}$CO(1–0) intensity ratio of 0.8 when expressed in temperature units (Bigiel et al. 2008; Carilli & Walter 2013). We note that our measured cloud size, velocity dispersion, and total CO luminosity and gas mass are extrapolated to zero intensity, as this approach is less affected by limited signal-to-noise and resolution effects (Rosolowsky & Leroy 2006).

The uncertainties on the measured and derived quantities are estimated using a bootstrap resampling technique. We note that the uncertainty on the adopted distance $D$ to NGC 5064 was not propagated through these uncertainties. This is because an uncertainty on the distance translates to a systematic (rather than random) scaling of some of the measured quantities (no effect on the others), i.e. $R_{\rm gal} \propto D$, $R_{\rm c} \propto D$, $L_{\rm CO(2-1)} \propto D^2$, $M_{\rm gas} \propto D^2$, and $M_{\rm vir} \propto D$ (and in later sections $\omega \propto D^{-1}$ and $\alpha_{\rm vir} \propto D^{-1}$). More detailed descriptions of the cloud properties can be found in Liu et al. (2021).

### 3.2 Probability distribution functions of GMC properties

The size ($R_{\rm c}$), molecular gas mass ($M_{\rm gas}$), observed velocity dispersion ($\sigma_{\rm obs,los}$), and molecular gas mass surface density ($\Sigma_{\rm gas} \equiv M_{\rm gas}/\pi R_{\rm c}^2$) distributions of the resolved clouds of NGC 5064 are shown in Fig. 5. In each panel, the black histogram shows the full resolved sample while the inset shows the cloud property as a function of galactocentric radius $R_{\rm gal}$. The back curve is a Gaussian fit to the histogram.

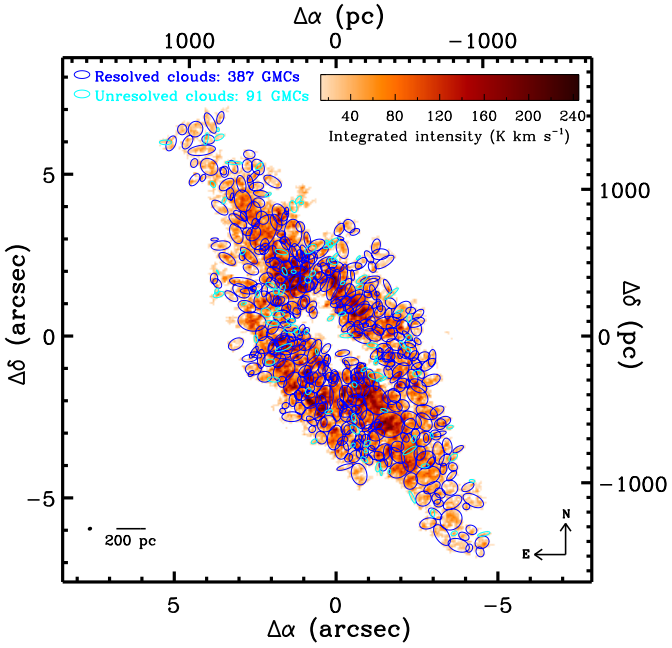


**Figure 4.** Molecular gas distribution of NGC 5064, created by masking out signal-free regions of the data cube using the CPROPSTOO-generated mask. This mask only includes regions with connected emission above 2 $\sigma_{\rm rms}$ and at least two adjacent channels above 3 $\sigma_{\rm rms}$. The 478 GMCs identified are each overlaid as an open ellipse whose major and minor axes have been extrapolated to the limit of perfect sensitivity but have not been corrected (i.e. deconvolved) for the finite spatial resolution. The resolved clouds are shown in blue, unresolved clouds in cyan. The synthesized beam of 0.14 arcsec $\times$ 0.12 arcsec ($31 \times 25$ pc$^2$) is shown in the bottom-left corner as a black solid ellipse.

MNRAS **541,** 3081–3100 (2025)

**Table 1.** NGC 5064 cloud properties.

| ID | RA (2000) (h:m:s) | Dec. (2000) (d:m:s) | $V_{lsr}$ (km s$^{-1}$) | $R_c$ (pc) | $\delta R_c$ (pc) | $\sigma_{obs,los}$ (km s$^{-1}$) | $\delta\sigma_{obs,los}$ (km s$^{-1}$) | $\sigma_{gs,los}$ (km s$^{-1}$) | $\delta\sigma_{gs,los}$ (km s$^{-1}$) | $L_{CO(2-1)}$ ($10^4$ K km s$^{-1}$ pc$^2$) | $\delta L_{CO(2-1)}$ ($10^4$ K km s$^{-1}$ pc$^2$) | $M_{gas}$ ($10^5$ M$_\odot$) | $\delta M_{gas}$ ($10^5$ M$_\odot$) | $\omega_{obs}$ (km s$^{-1}$ pc$^{-1}$) | $\delta\omega_{obs}$ (km s$^{-1}$ pc$^{-1}$) | $\phi_{rot}$ (°) | $\delta\phi_{rot}$ (°) | $R_{gal}$ (pc) |
|---|---|---|---|---|---|---|---|---|---|---|---|---|---|---|---|---|---|---|
| 1 | 13:19:00.3 | −47:54:26.1 | 2698.8 | 19.2 | 22.2 | 2.1 | 1.4 | 1.8 | 1.5 | 12.7 | 5.9 | 7.0 | 3.2 | 0.04 | 0.02 | 204.4 | 46.2 | 1358 |
| 2 | 13:19:00.3 | −47:54:24.8 | 2698.8 | 52.3 | 10.1 | 4.1 | 1.0 | 2.7 | 0.8 | 75.4 | 13.7 | 41.5 | 7.5 | 0.03 | 0.01 | 34.8 | 17.6 | 1700 |
| 3 | 13:19:00.3 | −47:54:26.0 | 2701.7 | 70.2 | 29.0 | 6.4 | 2.2 | 3.9 | 2.7 | 160.9 | 43.1 | 88.5 | 23.7 | 0.01 | 0.01 | 140.3 | 42.8 | 1451 |
| 4 | 13:19:00.3 | −47:54:25.2 | 2701.2 | 32.1 | 15.8 | 3.6 | 1.3 | 2.0 | 0.9 | 26.4 | 6.6 | 14.5 | 3.6 | 0.08 | 0.02 | 306.1 | 15.1 | 1596 |
| 5 | 13:19:00.4 | −47:54:24.8 | 2698.2 | 45.3 | 15.4 | 4.0 | 1.1 | 2.9 | 1.3 | 35.1 | 10.0 | 19.3 | 5.5 | 0.04 | 0.02 | 204.6 | 24.8 | 1764 |
| 6 | 13:19:00.3 | −47:54:25.9 | 2702.3 | 39.6 | 14.3 | 2.2 | 0.9 | 1.7 | 1.0 | 18.4 | 5.3 | 10.1 | 2.9 | 0.01 | 0.02 | 357.7 | 151.1 | 1569 |
| 7 | 13:19:00.4 | −47:54:25.2 | 2702.1 | 49.2 | 11.4 | 3.6 | 1.4 | 1.9 | 1.3 | 40.6 | 10.8 | 22.3 | 5.9 | 0.04 | 0.01 | 330.8 | 24.0 | 1681 |
| 8 | 13:19:00.2 | −47:54:26.8 | 2705.2 | 44.4 | 9.7 | 5.0 | 1.4 | 3.7 | 1.5 | 37.4 | 6.8 | 20.6 | 3.8 | 0.04 | 0.01 | 104.8 | 42.5 | 1217 |
| 9 | 13:19:00.2 | −47:54:26.6 | 2703.7 | 59.5 | 9.4 | 3.7 | 0.7 | 2.7 | 0.7 | 71.3 | 9.6 | 39.2 | 5.3 | 0.01 | 0.01 | 328.6 | 155.4 | 1275 |
| 10 | 13:19:00.3 | −47:54:26.3 | 2707.0 | 20.7 | 26.3 | 6.8 | 3.1 | 4.1 | 2.4 | 20.8 | 7.4 | 11.4 | 4.1 | 0.19 | 0.05 | 105.3 | 18.4 | 1463 |
| 11 | 13:19:00.2 | −47:54:26.0 | 2703.3 | 49.9 | 13.6 | 4.7 | 1.3 | 1.9 | 1.1 | 31.4 | 6.1 | 17.3 | 3.3 | 0.09 | 0.02 | 8.7 | 171.0 | 1355 |
| 12 | 13:19:00.3 | −47:54:25.5 | 2702.8 | 84.9 | 10.5 | 4.4 | 0.7 | 2.7 | 0.7 | 108.2 | 12.8 | 59.5 | 7.0 | 0.02 | 0.00 | 158.3 | 29.7 | 1564 |
| 13 | 13:19:00.4 | −47:54:25.3 | 2705.5 | 51.7 | 10.3 | 4.8 | 1.3 | 3.0 | 1.3 | 37.1 | 6.9 | 20.4 | 3.8 | 0.03 | 0.01 | 262.8 | 37.2 | 1804 |
| 14 | 13:19:00.3 | −47:54:24.6 | 2705.5 | 58.9 | 12.1 | 4.1 | 1.0 | 3.1 | 1.1 | 70.3 | 13.3 | 38.7 | 7.3 | 0.03 | 0.01 | 352.0 | 172.1 | 1705 |
| 15 | 13:19:00.3 | −47:54:26.5 | 2707.2 | – | – | 4.9 | 3.7 | 0.8 | 1.1 | 35.8 | 29.9 | 19.7 | 16.5 | – | – | – | – | 1368 |
| 16 | 13:19:00.3 | −47:54:26.2 | 2708.0 | 34.3 | 22.1 | 1.7 | 1.1 | 1.3 | 0.8 | 18.8 | 6.0 | 10.3 | 3.3 | 0.07 | 0.02 | 193.0 | 14.9 | 1349 |
| 17 | 13:19:00.3 | −47:54:27.0 | 2709.6 | – | – | 4.8 | 1.9 | 3.4 | 1.8 | 13.8 | 5.7 | 7.6 | 3.1 | – | – | – | – | 1238 |
| 18 | 13:19:00.4 | −47:54:25.2 | 2711.1 | – | – | 1.6 | 1.4 | 1.7 | 1.2 | 17.3 | 7.4 | 9.5 | 4.1 | – | – | – | – | 1856 |
| 19 | 13:19:00.3 | −47:54:25.1 | 2707.5 | – | – | 2.5 | 1.0 | 1.8 | 1.3 | 11.9 | 3.5 | 6.5 | 1.9 | – | – | – | – | 1606 |
| 20 | 13:19:00.3 | −47:54:25.1 | 2709.9 | – | – | 2.9 | 1.5 | 1.7 | 1.0 | 12.4 | 5.5 | 6.8 | 3.0 | – | – | – | – | 1590 |

*Note.* GMC properties (and uncertainties) as defined in the text. Spatially unresolved clouds have no $R_c$, $\omega_{obs}$, and $\phi_{rot}$. The full table is available online.

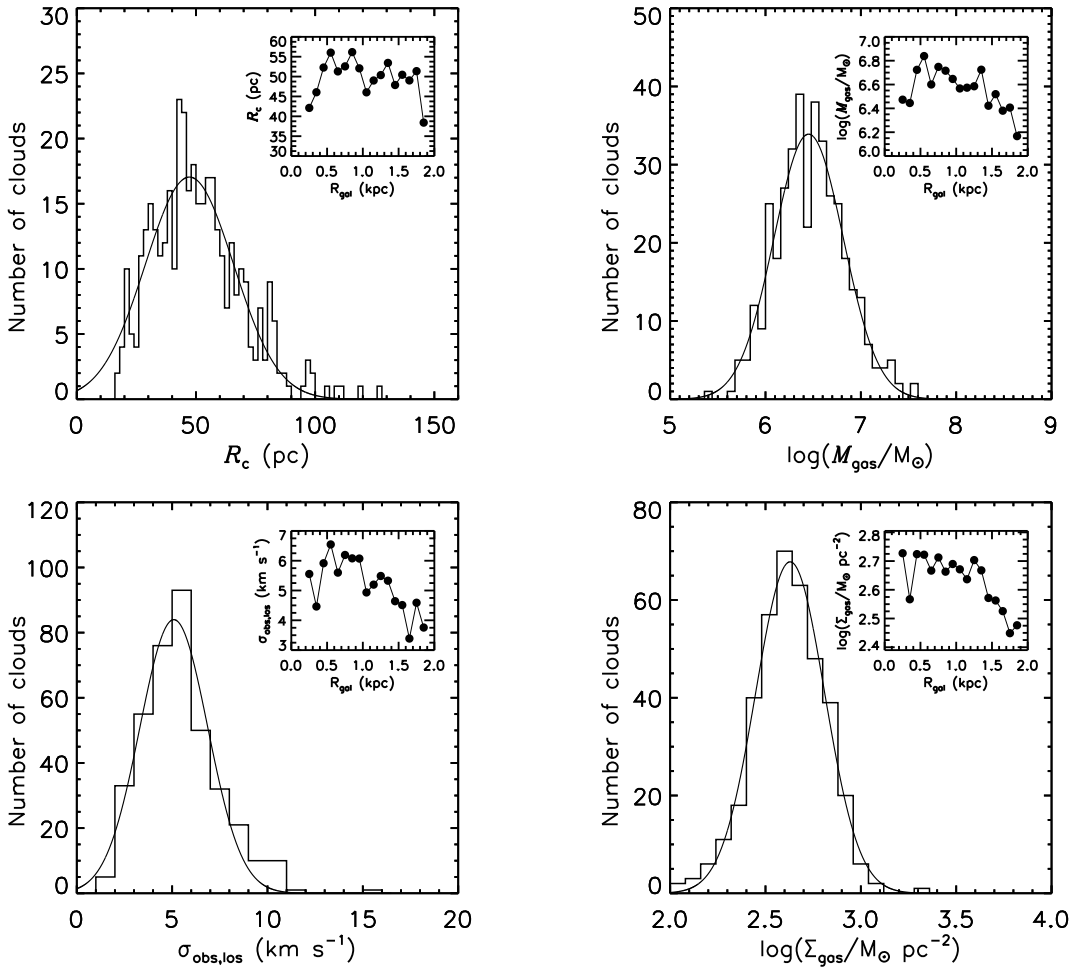


**Figure 5.** From left to right, top to bottom: distribution of the cloud sizes ($R_c$), molecular gas masses (log($M_{gas}$/M$_\odot$)), observed velocity dispersions ($\sigma_{obs,los}$), and molecular gas mass surface densities (log($\Sigma_{gas}$/M$_\odot$ pc$^{-2}$)) with a Gaussian fit overlaid, for the 387 resolved clouds of NGC 5064. Each inset shows the median of the plotted quantity as a function of galactocentric distance $R_{gal}$, measured in elliptical annuli of width $\Delta R_{gal} = 100$ pc.

The resolved clouds of NGC 5064 have sizes ranging from 17 to 127 pc, with a most probable size of $\approx 40$ pc (top-left panel of Fig. 5). A Gaussian fit to the size distribution yields a mean of $47 \pm 2$ pc. The sizes of the clouds of NGC 5064 are comparable to those of the clouds of the Galaxy disc (typical sizes $R_c = 30$–$50$ pc; e.g. Miville-Deschênes, Murray & Lee 2017b), Local Group galaxies (typical sizes $R_c = 20$–$70$ pc; e.g. Rosolowsky et al. 2003; Rosolowsky 2007; Hirota et al. 2011) and most late-type galaxies (typical sizes $R_c = 20$–$200$ pc; e.g. Donovan Meyer et al. 2012; Hughes et al. 2013; Rebolledo et al. 2015). The inset in the top-left panel of Fig. 5 reveals that the average cloud size does not depend strongly on the galactocentric distance, although clouds in the innermost regions ($R_{gal} \lesssim 500$ pc) and the farthest annulus probed ($R_{gal} \approx 2000$ pc) appear to have slightly smaller sizes than those at intermediate radii ($500 \lesssim R_{gal} \lesssim 2000$ pc).

The resolved clouds of NGC 5064 have molecular gas masses ranging from $2.5 \times 10^5$ to $3.2 \times 10^7$ M$_\odot$, with a most probable gas mass of $2.5 \times 10^6$ M$_\odot$ (top-right panel of Fig. 5). A Gaussian fit to the distribution of log($M_{gas}$/M$_\odot$) yields a mean of $6.5 \pm 0.03$. The clouds of NGC 5064 are generally quite massive, over 85 per cent (328/387) of the clouds having a gas mass $> 10^6$ M$_\odot$. The GMC population has a range of gas masses similar to those of the clouds of the MW (Milky Way) disc ($10^{4.5}$–$10^{7.8}$ M$_\odot$; Rice et al. 2016), M 64 ($10^{6.0}$–$10^{7.2}$ M$_\odot$; Rosolowsky & Blitz 2005), NGC 1068 ($10^{4.2}$–$10^{7.6}$ M$_\odot$; Tosaki et al. 2017), M 51 ($10^{5.0}$–$10^{7.5}$ M$_\odot$; Colombo et al. 2014), NGC 253 ($10^{6.3}$–$10^{7.8}$ M$_\odot$; Leroy et al. 2015) and the LMC ($10^{4.2}$–$10^{6.8}$ M$_\odot$; Hughes et al. 2010), but higher than those of the clouds of M 31 ($10^4$–$10^6$ M$_\odot$; Rosolowsky 2007), M 33 ($10^4$–$10^6$ M$_\odot$; Rosolowsky et al. 2003, 2007), and the SMC ($10^4$–$10^6$ M$_\odot$; Muller et al. 2010). As seen in the inset in the top-right panel of Fig. 5, the average cloud gas mass appears to slightly decrease with galactocentric distance at $R_{gal} \gtrsim 500$ pc. In addition, clouds close to the galactic centre (with distances $R_{gal} \lesssim 500$ pc) are also much less massive than clouds further away.

The resolved clouds of NGC 5064 have velocity dispersions ranging from 1.2 to 15.9 km s$^{-1}$, with a most common velocity dispersion of $\approx 6$ km s$^{-1}$ (bottom-left panel of Fig. 5). A Gaussian fit to the velocity dispersion distribution yields a mean of $5.1 \pm 0.2$ km s$^{-1}$. The velocity dispersions of the clouds of NGC 5064 are comparable to those of clouds with similar sizes in the MW disc and Local Group galaxies (typical velocity dispersion 3–4 km s$^{-1}$; e.g. Rosolowsky et al. 2003; Rosolowsky 2007; Fukui et al. 2008; Muller et al. 2010). The inset in the bottom-left panel of Fig. 5 shows that the average velocity dispersion strongly decreases with galactocentric distance beyond $\approx 1000$ pc.

The resolved clouds of NGC 5064 have molecular gas mass surface densities ranging from 95 to $2.0 \times 10^3$ M$_\odot$ pc$^{-2}$, with a most common gas mass surface density of $\approx 400$ M$_\odot$ pc$^{-2}$. A Gaussian fit

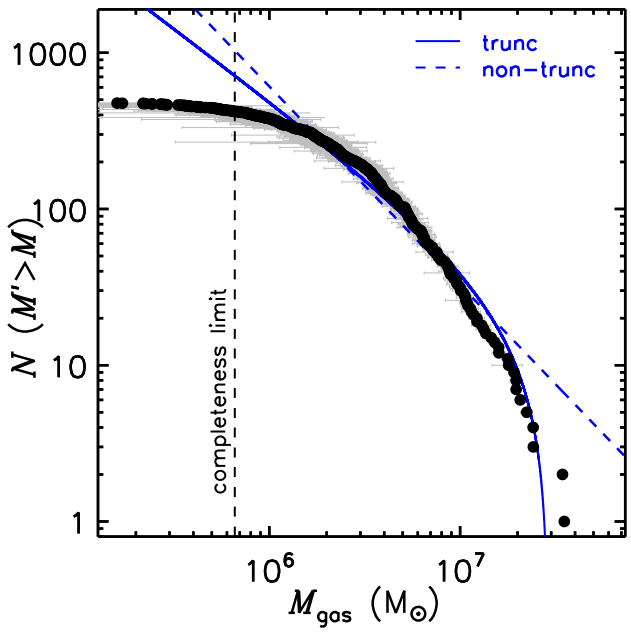


**Figure 6.** Cumulative molecular gas mass function of all the clouds of NGC 5064. Truncated (solid line) and non-truncated (dashed line) power-law fits are overlaid in blue. The mass completeness limit is indicated by a black vertical dashed line.

to the $\log(\Sigma_{gas}/M_\odot\ pc^{-2})$ distribution yields a mean of $2.56 \pm 0.02$. The average gas mass surface density of the clouds of NGC 5064 is slightly larger than that of the clouds of the Galaxy disc, LMC, M 33, and M 64 ($\langle\Sigma_{gas}\rangle \approx 100\ M_\odot\ pc^{-2}$; Rosolowsky et al. 2003; Rosolowsky & Blitz 2005; Heyer et al. 2009; Hughes et al. 2010; Lombardi, Alves & Lada 2010; Miville-Deschênes et al. 2017b). The gas mass surface densities of individual resolved clouds of NGC 5064 vary by about one order of magnitude. As shown in the inset in the bottom-right panel of Fig. 5, the average gas mass surface density of the resolved clouds decreases steadily with galactocentric distance, particularly at large galactocentric distances ($R_{gal} \gtrsim 1300$ pc).

Overall, the clouds of NGC 5064 have properties almost indistinguishable from those of the clouds of the MW disc and Local Group galaxies (e.g. LMC, M 31, M 33, and M 64). Clouds close to the galaxy centre ($R_{gal} \lesssim 500$ pc) tend to have smaller sizes and molecular gas masses, both increasing with galactocentric distance. Conversely, for clouds at larger galactocentric distances ($R_{gal} \gtrsim 500$ pc), the sizes, gas masses, velocity dispersions, and gas mass surface densities all exhibit a weak declining trend with increasing galactocentric distance.

### 3.3 GMC mass functions

The mass function of the GMCs of NGC 5064 can be directly calculated from our data (Fig. 6). We use here the molecular gas masses, as they can be evaluated for all clouds (including spatially unresolved clouds) and make no assumption about the dynamical states of the clouds. The cumulative mass function is fit with both a power-law function

$$N(M' > M) = \left(\frac{M}{M_0}\right)^{\gamma+1}, \quad (1)$$

where $N(M' > M)$ is the number of clouds with a mass greater than $M$, $M_0$ sets the normalization, and $\gamma$ is the power-law index, and a truncated power-law function

$$N(M' > M) = N_0 \left[\left(\frac{M}{M_0}\right)^{\gamma+1} - 1\right], \quad (2)$$

where $M_0$ is now the cut-off mass and $N_0$ the number of clouds with a mass $M > 2^{1/(\gamma+1)} M_0$. The fits are performed using the 'error in variable' method of Rosolowsky (2005) for clouds more massive than the mass completeness limit of $M_{comp} = 6.5 \times 10^5\ M_\odot$ (shown as a black vertical dashed line in Fig. 6). This mass completeness limit $M_{comp}$ is estimated using the minimum luminous mass of resolved clouds ($M_{min} = 2.7 \times 10^5\ M_\odot$) and the observational sensitivity, i.e. $M_{comp} \equiv M_{min} + 10\delta_M$, where $\delta_M \approx 3.8 \times 10^4\ M_\odot$ is the noise contribution to the mass and is estimated by multiplying our $1\sigma$ column density sensitivity limit of $43.7\ M_\odot\ pc^{-2}$ by the synthesized beam area of $882\ pc^2$. The uncertainties of the fitting parameters are estimated via bootstrapping.

The truncated power law fits better the cumulative mass function, especially at the high-mass end ($M_{gas} \gtrsim 10^7\ M_\odot$). We therefore only report the best-fitting parameters of the truncated power law, with a best-fitting slope $\gamma = -1.92 \pm 0.07$, consistent with $\gamma = -2$. This slope is identical or similar to that of the cumulative mass function of the clouds of the outer Galaxy ($\gamma = -2.2 \pm 0.1$; Rice et al. 2016), the outer regions of M 33 ($\gamma = -2.1 \pm 1$; Rosolowsky et al. 2007; Gratier et al. 2012; Corbelli et al. 2017), M 51 ($\gamma = -2.3 \pm 0.1$; Colombo et al. 2014) and the early-type galaxies NGC 4526 ($\gamma = -2.39 \pm 0.03$; Utomo et al. 2015) and NGC 4429 ($\gamma = -2.18 \pm 0.12$; Liu et al. 2021), but it is smaller than that of the cumulative mass function of the clouds of the inner Galaxy ($\gamma = -1.6 \pm 0.1$; Rice et al. 2016), the spiral arms of M 51 ($\gamma = -1.79 \pm 0.09$; Colombo et al. 2014), NGC 300 ($\gamma = -1.80 \pm 0.07$; Faesi, Lada & Forbrich 2016), NGC 1068 ($\gamma = -1.25 \pm 0.07$; Tosaki et al. 2017), and the overall cloud population of Local Group galaxies ($\gamma \approx -1.7$; Blitz et al. 2007).

The best-fitting cut-off mass of our truncated power-law fit to all the clouds of NGC 5064 is $M_0 = (2.93 \pm 0.39) \times 10^7\ M_\odot$, comparable to that of the clouds of the inner Galaxy ($M_0 = (1.0 \pm 0.2) \times 10^7\ M_\odot$; Rice et al. 2016), NGC 1068 ($M_0 = (5.9 \pm 0.6) \times 10^7\ M_\odot$; Tosaki et al. 2017) and M 51 ($M_0 = (1.8 \pm 0.3) \times 10^7\ M_\odot$; Colombo et al. 2014), but significantly higher than that of the clouds of the inner regions of M 33 ($M_0 = (7.4 \pm 0.5) \times 10^5\ M_\odot$; Rosolowsky et al. 2007), the outer regions of M 33 ($M_0 = (3.4 \pm 1.2) \times 10^6\ M_\odot$; Rosolowsky et al. 2007), and the outer Galaxy ($M_0 = (1.5 \pm 0.5) \times 10^6\ M_\odot$; Rice et al. 2016).

Overall, we find the truncated power law provides a better fit, particularly for higher-mass clouds. The best-fitting slope and cut-off mass generally align with trends observed in other galaxies.

## 4 CLOUD DYNAMICAL STATES

### 4.1 Larson's relations

Larson (1981) uncovered three empirical scaling relations between the sizes, linewidths (velocity dispersions), and luminosities of GMCs, that have since become the standard tool to compare the dynamical states of molecular cloud populations (e.g. Blitz et al. 2007; Hughes et al. 2013). The first relation, known as the size–linewidth relation, takes the form of a power law. This relation is often interpreted to suggest the presence of turbulence within clouds (e.g. Lequeux 2005, chap. 13). One form of the second relation is a power-law relation between the cloud luminosities and sizes. The third relation is derived from the first two, and can be expressed as

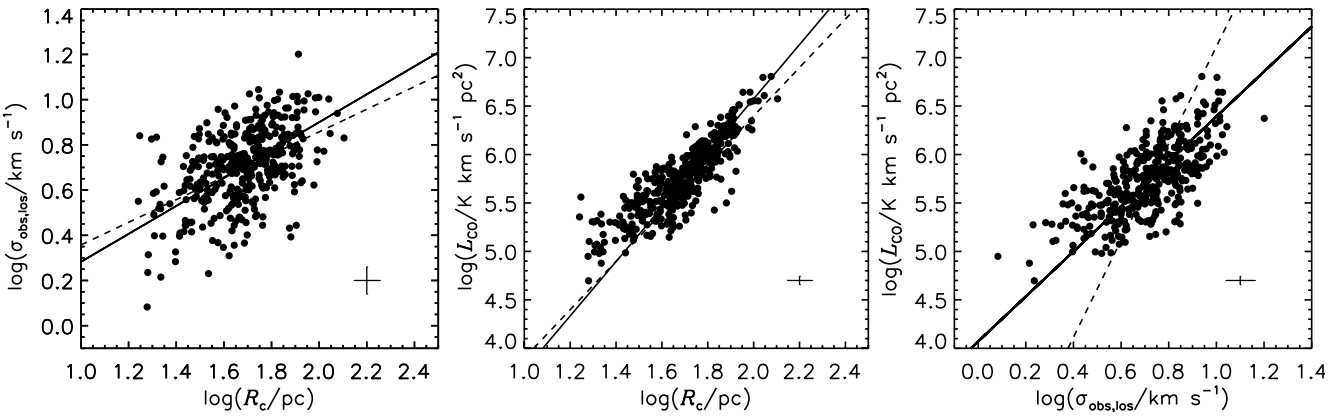


**Figure 7.** Correlations between the properties of the resolved clouds of NGC 5064 (i.e. Larson's relations). The best-fitting power laws are shown as black solid lines, while Larson's relations for MW disc clouds are shown as black dashed lines. The typical uncertainty is shown as a cross in the bottom-right corner of each panel. Left: size–linewidth (observed velocity dispersion) relation. Middle: luminosity–size relation. Right: luminosity–linewidth (observed velocity dispersion) relation.

a power-law relation between the cloud luminosities (or molecular gas masses) and velocity dispersions.

Larson's relations for the resolved clouds of NGC 5064 are plotted in Fig. 7. Luminosity ($L_{\rm CO}$) is plotted instead of molecular gas mass as $L_{\rm CO(2-1)}$ is a measured quantity (free of assumption). For comparison, we also plot the corresponding Larson relations of MW disc clouds as black dashed lines: $\left(\frac{\sigma_{\rm obs,los}}{\rm km\ s^{-1}}\right) \approx 0.72 \left(\frac{R_{\rm c}}{\rm pc}\right)^{\frac{1}{2}}$, $\left(\frac{L_{\rm CO(2-1)}}{\rm K\ km\ s^{-1}\ pc^2}\right) \approx 25 \left(\frac{R_{\rm c}}{\rm pc}\right)^{\frac{5}{2}}$, and $\left(\frac{L_{\rm CO(2-1)}}{\rm K\ km\ s^{-1}\ pc^2}\right) \approx 130 \left(\frac{\sigma_{\rm obs,los}}{\rm km\ s^{-1}}\right)^{5}$ (Solomon et al. 1987).

For the resolved clouds of NGC 5064, there is a moderate correlation between size and linewidth (observed velocity dispersion), with a Spearman rank correlation coefficient $r_{\rm sp} = 0.46$ (left panel of Fig. 7). Our best fit yields

$$\left(\frac{\sigma_{\rm obs,los}}{\rm km\ s^{-1}}\right) = 0.48^{+0.18}_{-0.13} \left(\frac{R_{\rm c}}{\rm pc}\right)^{0.6\pm0.1}, \quad (3)$$

with a power-law index slightly steeper than that of MW clouds. The best-fitting power-law index is comparable to that of the clouds of the MW disc ($\approx 0.5$; Solomon et al. 1987), M 31 ($0.7 \pm 0.2$; Rosolowsky 2007), and the Local Group galaxies studied by Bolatto et al. (2008; $0.60 \pm 0.10$), but it is shallower than that of the clouds of the early-type galaxy NGC 4429 ($0.82 \pm 0.13$; Liu et al. 2021) and steeper than that of the clouds of M 33 ($0.45 \pm 0.02$; Rosolowsky et al. 2003). Our best-fitting scale factor of $0.48^{+0.18}_{-0.13}$ (zero-point of $-0.32 \pm 0.14$ in logarithmic scale) is comparable to that of the clouds of the MW ($1.0 \pm 0.1$; Solomon et al. 1987), NGC 4429 ($0.50^{+0.24}_{-0.16}$; Liu et al. 2021), M 31 ($0.31^{+0.31}_{-0.16}$; Rosolowsky 2007), and the Bolatto et al. (2008) clouds ($0.44^{+0.18}_{-0.13}$), but it is much lower than that of the clouds of the MW Central Molecular Zone ($5.5 \pm 1.0$; Kauffmann et al. 2017).

The middle panel of Fig. 7 reveals a strong correlation between the luminosities and sizes of the resolved clouds of NGC 5064, with $r_{\rm sp} = 0.86$. The best-fitting power law is

$$\left(\frac{L_{\rm CO(2-1)}}{\rm K\ km\ s^{-1}\ pc^2}\right) = 12.6^{+6.5}_{-4.3} \left(\frac{R_{\rm c}}{\rm pc}\right)^{2.8\pm0.1}. \quad (4)$$

The power-law index is similar to that of the clouds of the MW disc ($\approx 2.5$; Solomon et al. 1987) and late-type galaxies in the Local Group ($2.54 \pm 0.20$; Bolatto et al. 2008), but it is steeper than that of the clouds of the LMC ($1.88 \pm 0.08$; Hughes et al. 2010) and the early-type galaxies NGC 4526 ($1.6 \pm 0.1$; Utomo et al. 2015) and NGC 4429 ($1.5 \pm 0.1$; Liu et al. 2021). The best-fitting scale factor of $12.6^{+6.5}_{-4.3}$ (zero-point of $1.10 \pm 0.18$ in logarithmic scale) is comparable to that of the clouds of the MW disc ($\approx 25$; Solomon et al. 1987), the LMC ($24.5^{+7.8}_{-5.9}$; Hughes et al. 2010), and late-type galaxies in the Local Group ($7.8^{+6.9}_{-3.7}$; Bolatto et al. 2008), but it is much lower than that of the clouds of NGC 4429 ($501^{+293}_{-185}$; Liu et al. 2021) and NGC 4526 ($381^{+636}_{-238}$; Utomo et al. 2015). At a given size, the clouds of NGC 5064 thus appear to be as luminous in CO as typical clouds of the MW disc. The cloud molecular gas mass surface densities are therefore also similar in both galaxies.

In the right panel of Fig. 7, a moderate correlation is present between the luminosities and linewidths (observed velocity dispersions) of the resolved clouds of NGC 5064, with $r_{\rm sp} = 0.67$. The best-fitting power law is

$$\left(\frac{L_{\rm CO(2-1)}}{\rm K\ km\ s^{-1}\ pc^2}\right) = 8300^{+3200}_{-2300} \left(\frac{\sigma_{\rm obs,los}}{\rm km\ s^{-1}}\right)^{2.5\pm0.2}. \quad (5)$$

The power-law index is slightly shallower than that of the clouds of the MW disc ($\approx 4.0$; Bolatto et al. 2008), Local Group galaxies ($3.35 \pm 0.19$; Bolatto et al. 2008), and the early-type galaxy NGC 4526 ($3.2 \pm 0.5$; Utomo et al. 2015), but it is steeper than that of the clouds of the early-type galaxy NGC 4429 ($1.45 \pm 0.09$; Liu et al. 2021). Our best-fitting scale factor of $8300^{+3200}_{-2300}$ (zero-point of $3.90 \pm 0.14$ in logarithmic scale) is much larger than that of the Bolatto et al. (2008) clouds ($645^{+165}_{-132}$) and is larger than that of the clouds of the early-type galaxies NGC 4429 ($2820^{1260}_{-870}$; Liu et al. 2021) and NGC 4526 ($2259^{+1033}_{-709}$; Utomo et al. 2015).

In summary, the size–linewidth and luminosity–size relations are similar to those in the Milky Way and Local Group galaxies, though the luminosity–linewidth relation is slightly shallower. Our results suggest that the clouds in NGC 5064 are similar to those in the Milky Way disc, indicating comparable turbulence and molecular gas surface densities.

### 4.2 Virial parameter

To further probe the dynamical states of the resolved clouds of NGC 5064, we compare each cloud's virial mass ($M_{\rm obs,vir} \equiv 5\sigma^2_{\rm obs,los} R_{\rm c}/G$, where $G$ is the gravitational constant and the factor of 5 assumes a spherical geometry with uniform mass volume density) to its

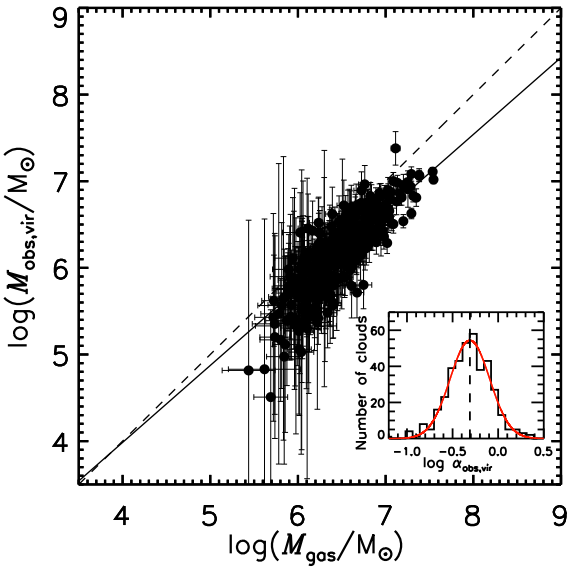


**Figure 8.** Comparison of the virial masses $M_{\rm obs,vir}$ (calculated using the observed velocity dispersions $\sigma_{\rm obs,los}$) and the molecular gas masses $M_{\rm gas}$ of the resolved clouds of NGC 5064. The black solid line shows the best-fitting power-law relation, while the black dashed line shows the 1 : 1 relation. The inset shows the number distribution of the observed virial parameters $\alpha_{\rm obs,vir}$, whose mean is $\langle\log(\alpha_{\rm obs,vir})\rangle = -0.31^{+0.03}_{-0.02}$ ($\langle\alpha_{\rm obs,vir}\rangle = 0.48 \pm 0.03$). The best-fitting lognormal function is overlaid in red.

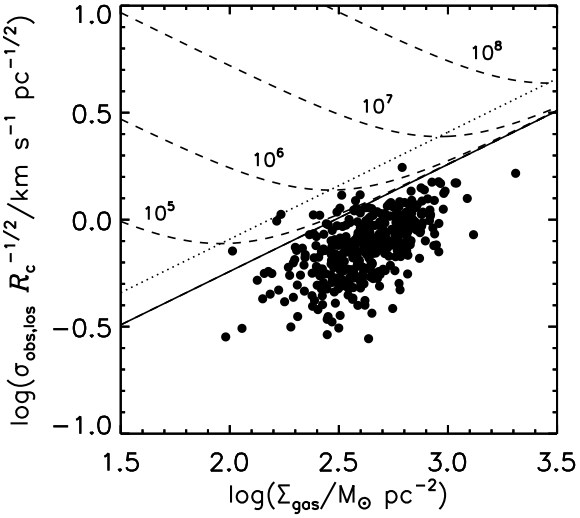


**Figure 9.** Correlation between $\sigma_{\rm obs,los} R_{\rm c}^{-\frac{1}{2}}$ and $\Sigma_{\rm gas}$ of the resolved clouds of NGC 5064. The solid diagonal line represents the solution for simple virial equilibrium (i.e. $\alpha_{\rm obs,vir} = 1$), while the dotted diagonal line represents the solution for only marginally gravitationally bound clouds (i.e. $\alpha_{\rm obs,vir} = 2$). The dashed V-shaped curves show solutions for pressure-bound clouds at a variety of external pressures (actually $P_{\rm ext}/k$, where $k$ is Boltzmann's constant, labelled in units of K cm$^{-3}$).

molecular gas mass and in turn calculate the virial parameter $\alpha_{\rm vir} \equiv \frac{M_{\rm vir}}{M_{\rm gas}}$. Gravitationally bound clouds should have $\alpha_{\rm vir} \leq 1$, while gravitationally unbound (i.e. transient or pressure-bound) clouds should have $\alpha_{\rm vir} \geq \alpha_{\rm crit} = 2$. Indeed, we note that a critical parameter $\alpha_{\rm crit} = 2$ is often regarded as the threshold between gravitationally bound and unbound objects (Kauffmann et al. 2017).

Fig. 8 reveals that most (368/387) resolved clouds have an observed virial parameter ($\alpha_{\rm obs,vir} \equiv \frac{M_{\rm obs,vir}}{M_{\rm gas}}$) smaller than one. The resolved clouds of NGC 5064 have a mean observed virial parameter $\langle\log(\alpha_{\rm obs,vir})\rangle = -0.31^{+0.03}_{-0.02}$ ($\langle\alpha_{\rm obs,vir}\rangle = 0.48 \pm 0.03$), smaller than that of most other galaxies ($\langle\alpha_{\rm vir}\rangle > 1 - 2$; e.g. Bolatto et al. 2008; Heyer et al. 2009; Sun et al. 2018; Wong et al. 2019). These small virial parameters suggest that most clouds are strongly self-gravitating and susceptible to gravitational collapse and star formation (e.g. Kauffmann, Pillai & Zhang 2013), and indeed NGC 5064 is forming stars quite efficiently ($t_{\rm dep} \approx 0.5$ Gyr; see Section 2.1).

We also present the $\sigma_{\rm obs,los} R_{\rm c}^{-\frac{1}{2}} - \Sigma_{\rm gas}$ relation in Fig. 9, a variation on Larson's relations allowing to easily gauge the possible impact of external pressure. If the data points cluster around the dashed V-shaped curves $\sigma_{\rm obs,los} R_{\rm c}^{-\frac{1}{2}} = \sqrt{\frac{\pi G \Sigma_{\rm gas}}{5} + \frac{4}{3}\frac{P_{\rm ext}}{\Sigma_{\rm gas}}}$ (Field, Blackman & Keto 2011) rather than the diagonal lines ($\alpha_{\rm obs,vir} = 1$ and 2), external pressure ($P_{\rm ext}$) must play an important role to confine the clouds (i.e. the clouds are unlikely to be gravitationally bound). Conversely, if the data points follow the diagonal lines ($P_{\rm ext} = 0$), clouds are likely to be gravitationally bound. In NGC 5064, most data points (373/387) lie below the $\alpha_{\rm obs,vir} = 1$ solid diagonal line, implying the resolved clouds of NGC 5064 are bound by self gravity rather than external pressure.

In general, most clouds (368 out of 387) exhibit an observed virial parameter significantly less than one ($\langle\alpha_{\rm obs,vir}\rangle = 0.48 \pm 0.03$), indicating they are primarily self-gravitating. Additionally, analysis of the $\sigma_{\rm obs,los} R_{\rm c}^{-\frac{1}{2}} - \Sigma_{\rm gas}$ relation shows that most clouds lie below the $\alpha_{\rm obs,vir} = 1$ line, further suggesting that self-gravity, rather than external pressure, is the dominant force in confining these clouds. We will explore the unusually low virial parameter and its potential link to the CO conversion factor in Section 6.3.

## 5 CLOUD KINEMATICS

### 5.1 Cloud velocity gradients

As many previous studies have shown, clouds exhibit internal velocity gradients that can normally be fit by solid-body rotation (e.g. Blitz 1993; Phillips 1999; Rosolowsky et al. 2003; Rosolowsky 2007; Utomo et al. 2015). We thus fit the first-moment (intensity-weighted mean line-of-sight velocity) map of each cloud with a plane using a modified version of the LTS_PLANEFIT code of Cappellari et al. (2013). The projected angular velocity $\omega_{\rm obs}$ (i.e. the projected magnitude of the velocity gradient) and the position angle of the rotation axis $\theta_{\rm rot}$ of each cloud are then calculated from the best-fitting plane coefficients:

$$\omega_{\rm obs} = \sqrt{a^2 + b^2}\ , \tag{6}$$

$$\theta_{\rm rot} = \tan^{-1}(b/a)\ , \tag{7}$$

where $a$ and $b$ are the best-fitting projected velocity gradients along the $x-$ and the $y-$axis on the sky, respectively ($v(x, y) = ax + by + c$, where $c$ is a constant). We note that our measurement of $\omega_{\rm obs}$ underestimates the true angular velocity $\omega_{\rm true}$, i.e. $\omega_{\rm true} = \omega_{\rm obs}/\sin i$, where $i$ is the inclination of the given cloud along the line of sight.

The velocity maps of the clouds of NGC 5064 can generally be well fitted by solid-body rotation. We show one example of our plane fitting in the top panel of Fig. 10, where the mean intensity-weighted line-of-sight velocity of each spaxel within the cloud is also plotted against that spaxel's perpendicular distance from the rotation axis (determined via plane fitting). As expected, the data points of a cloud in solid-body rotation closely follow a straight line.

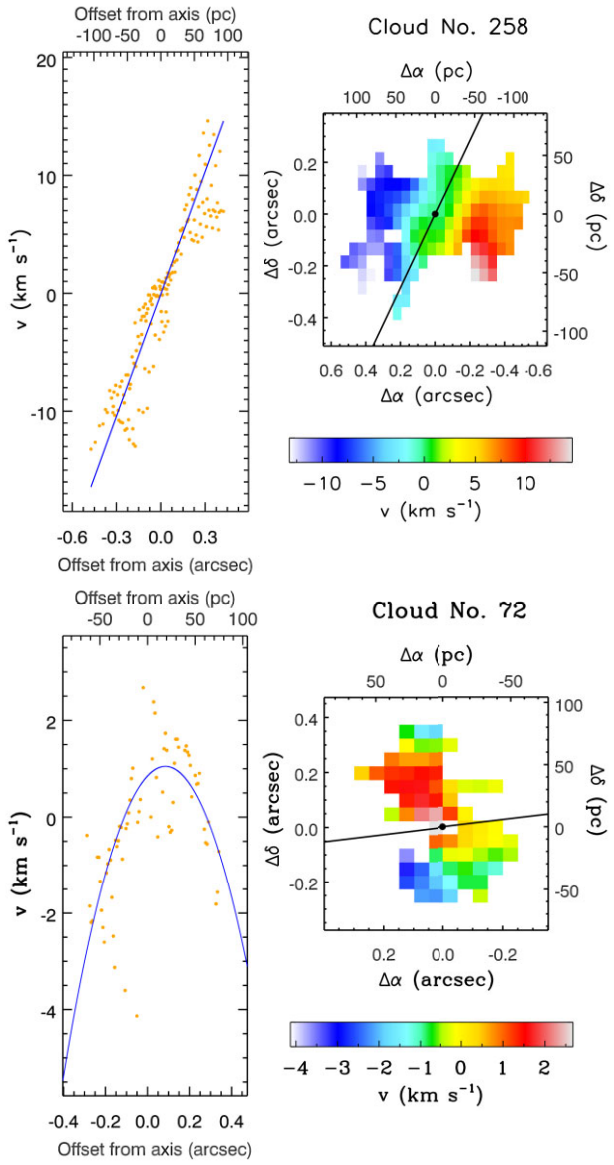


**Figure 10.** Examples of internal kinematics of GMCs of NGC 5064. The right panels show the intensity-weighted mean line-of-sight velocity map of each cloud. The best-fitting rotation axes (determined via plane fitting; see Section 5.1) are overplotted as solid black lines, the best-fitting centres as solid black circles. The left panels show the intensity-weighted mean line-of-sight velocity of each spaxel of each cloud as a function of the perpendicular distance of that spaxel from the best-fitting rotation axis (orange data points). The upper panel (cloud no. 258) shows a common case where the velocity map of the cloud is well fitted by solid-body rotation. A straight-line fit to the data is overlaid in blue for illustrative purposes. The lower panel (cloud no. 72) shows a rare case where the velocity map of the cloud is instead well-fitted by a parabolic function. A parabolic fit to the data is overlaid in blue for illustrative purposes.

There are also a few rare cases where the velocity map of a cloud is better fitted by a parabolic function (see the bottom panel of Fig. 10). Under external influences such as bow shocks, gas in the outer parts of a cloud can gain momentum relative to its centre and display differential rotation (Kane & Clemens 1997; Utomo et al. 2015). As a result, data points in the velocity versus perpendicular distance plot can follow a parabolic shape.

The results of the plane fits to the velocity maps of the clouds of NGC 5064 ($\omega_{\rm obs}$ and $\phi_{\rm rot}$) are listed in Table 1. The angular velocities $\omega_{\rm obs}$ of the 387 resolved clouds range from 0.01 to 0.23 km s$^{-1}$ pc$^{-1}$, with an average of $\approx$ 0.07 km s$^{-1}$ pc$^{-1}$. This is comparable to the angular velocities measured for clouds of the Milky Way ($\approx$ 0.1 km s$^{-1}$ pc$^{-1}$; Blitz 1993; Phillips 1999; Imara & Blitz 2011), M 33 ($\approx$ 0.15 km s$^{-1}$ pc$^{-1}$; Rosolowsky et al. 2003; Imara et al. 2011a; Braine et al. 2018), M 31 (0–0.2 km s$^{-1}$ pc$^{-1}$; Rosolowsky 2007) and M 51 ($\approx$ 0.05 km s$^{-1}$ pc$^{-1}$; Braine et al. 2020), but it is smaller than those of the clouds of the early-type galaxies NGC 4526 (0.04–1.2 km s$^{-1}$ pc$^{-1}$; Utomo et al. 2015) and NGC 4429 (0.05–0.91 km s$^{-1}$ pc$^{-1}$; Liu et al. 2021).

### 5.2 Cloud rotational axes

It is interesting to see how the rotational axes of individual clouds are (mis)aligned with respect to the large-scale galaxy rotation. Simulations and observations show that the angular momentum vectors of large numbers of clouds can be anti-aligned with respect to that of the large-scale galaxy rotation, i.e. a large number of clouds can have retrograde internal rotation (e.g. Koda et al. 2006; Tasker & Tan 2009). The fraction of retrograde clouds $f_{\rm retro}$ can be a useful diagnostic of the surrounding environments of the clouds (e.g. Dobbs 2008; Braine et al. 2020). We compare in Fig. 11 the projected orientations of the rotational axes of the resolved clouds of NGC 5064 with those of the isovelocity contours of the galaxy (i.e. the large-scale galaxy rotation). Even a cursory examination reveals that the (projected) angular momentum vectors appear to be randomly distributed, with no clear evidence of alignment with the isovelocity contours.

We also calculate the angle $|\Delta\phi|$ between the observed (projected) rotational axis of a cloud and the local isovelocity contour on the same spatial scale as the cloud. This results in 257 retrograde clouds ($90^\circ < |\Delta\phi| \leq 180^\circ$) and 130 prograde clouds ($0^\circ \leq |\Delta\phi| < 90^\circ$), i.e. about 67 per cent or two-thirds of the resolved clouds of NGC 5064 have retrograde internal rotation. This fraction of retrograde clouds is significantly larger than those observed in M 33, M 31, and M 51 (20–30 per cent; Rosolowsky 2007; Braine et al. 2018, 2020). We will discuss mechanisms that may explain this high retrograde fraction in Section 6.1.

We note that the circular velocity curve and galaxy parameters used to derive the isovelocity contours of NGC 5064 are taken from an existing axisymmetric mass model by Onishi et al. (in prep.). The model was constrained by modelling the molecular gas kinematics using the `Kinematic Molecular Simulation` (KinMS) package (Davis et al. 2013; Davis, Zabel & Dawson 2020), and was primarily used to constrain the mass of the central supermassive black hole. Parameters of the model include the stellar mass distribution, stellar mass-to-light ratio, black hole mass and disc position (spatially and in velocity) and orientation (position angle and inclination), and the stellar mass distribution was parametrized by a multi-Gaussian expansion (Cappellari 2002) fit to a *Hubble Space Telescope (HST)* NICMOS F160W image. The free parameters were constrained by fitting the model to the observed gas kinematics assuming the object is axisymmetric (in the central parts where CO is located), the gas is in circular rotation and the mass-to-light ratio is spatially uniform (see Davis et al. 2018 for details of the fitting procedures). The masses of the molecular gas and potential dark matter were not included in the model, as they are small compared to those of the black hole and stars. The resulting model yields a best-fitting inclination of 70.8 and a kinematic position angle of 35°, both adopted to calculate the line-of-sight projections of the best-fitting

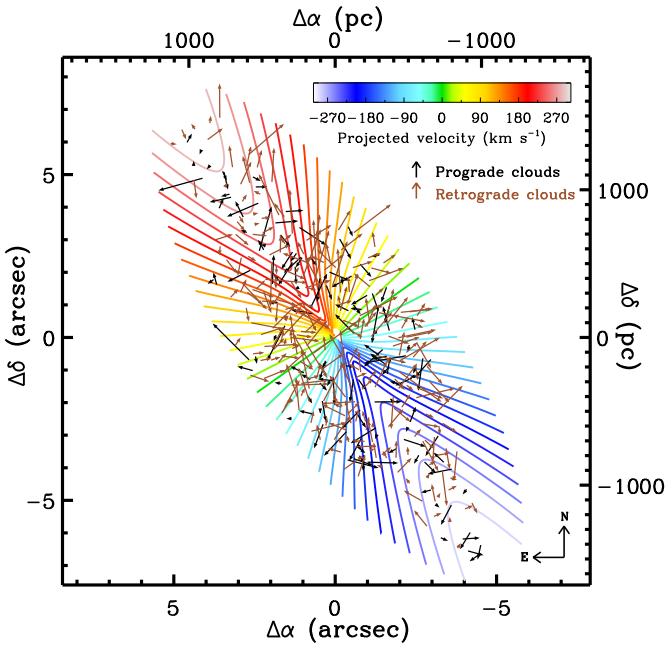


**Figure 11.** Projected isovelocity contours of NGC 5064 (colour-coded by their velocities and derived from the gas dynamical model described in Section 5.3) overlaid with the projected angular momentum vectors of the resolved clouds (arrows; black for prograde clouds, brown for retrograde clouds). The length of each arrow represents the magnitude of the velocity gradient (i.e. $\omega_{\rm obs}$). There is no tendency for the projected angular momenta to be tangential to the isovelocity contours, suggesting that the observed velocity gradients do not arise from the large-scale galaxy rotation.

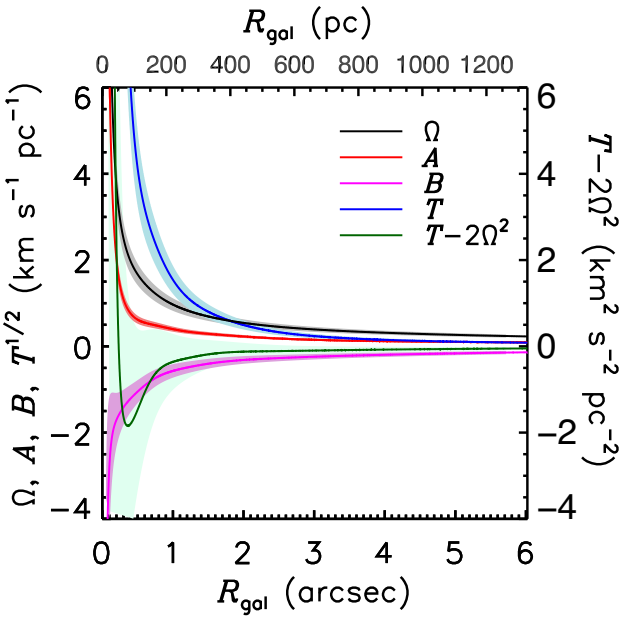


**Figure 12.** Galactocentric distance dependence of the orbital circular angular velocity Ω (black curve), Oort's constants $A$ (red curve) and $B$ (purple curve) and the tidal acceleration parameter $T$ (blue curve) of NGC 5064. The coloured envelope around each curve indicates the $\pm1\sigma$ uncertainties.

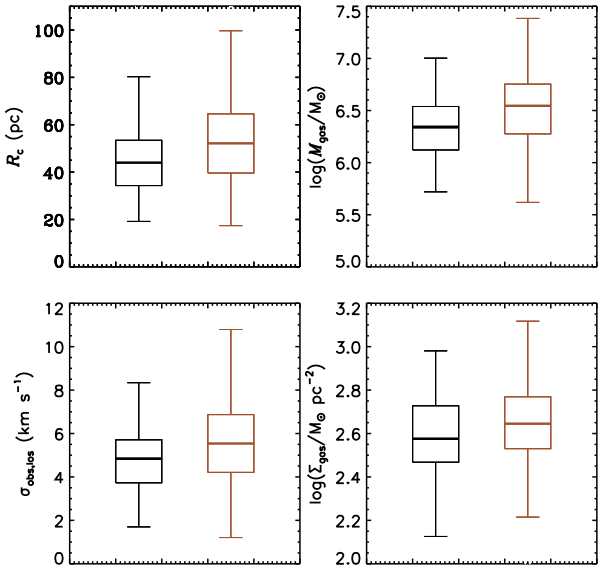


**Figure 13.** Box plots of the cloud properties of prograde clouds (black) and retrograde clouds (brown), showing the interquartile ranges (boxes), medians (thick horizontal lines) and lower and upper limits (upper and lower whiskers) of cloud size $R_{\rm c}$ (top left), molecular gas mass $M_{\rm gas}$ (top right), velocity dispersion $\sigma_{\rm obs,los}$ (bottom left), and molecular gas mass surface density $\Sigma_{\rm gas}$ (bottom right).

gas circular velocities in Fig. 11 and the cloud deprojected distances from the galaxy centre ($R_{\rm gal}$).

For reference, we show in Fig. 12 the circular orbital angular velocity Ω, Oort's constants $A$ and $B$ and the tidal acceleration per unit length in the radial direction $T \equiv -R\frac{d\Omega^2}{dR}$ (e.g. Stark & Blitz 1978) as functions of the galactocentric distance $R_{\rm gal}$ in NGC 5064.

It is interesting to compare the physical properties of the prograde and retrograde clouds. The boxes in the panels of Fig. 13 highlight the main statistical trends of each cloud property (size $R_{\rm c}$, molecular gas mass $M_{\rm gas}$, velocity dispersion $\sigma_{\rm obs,los}$ and molecular gas mass surface density $\Sigma_{\rm gas}$), including the interquartile range (upper and lower

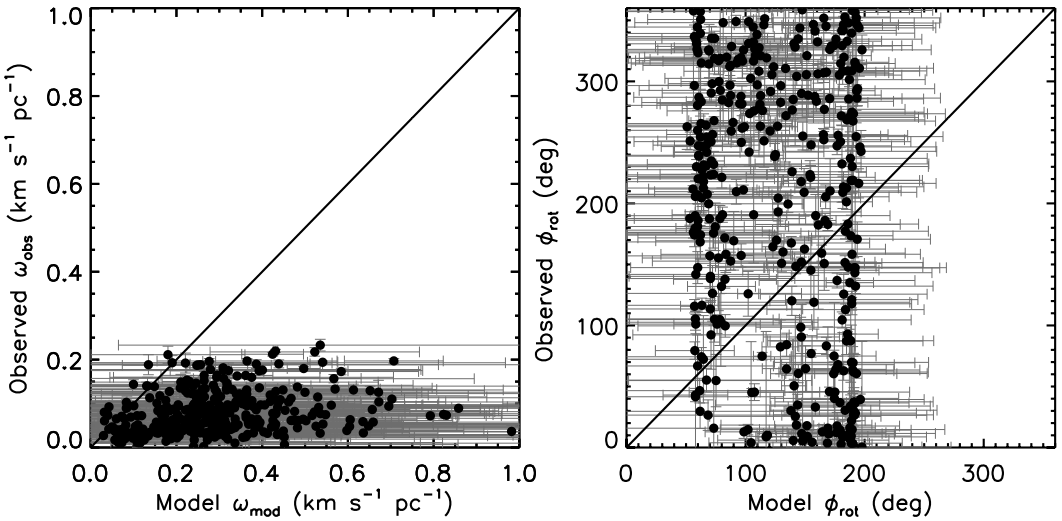


**Figure 14.** Correlations between the modelled and observed projected angular velocities $\omega_{obs}$ (left panel) and rotation axis position angles $\phi_{rot}$ (right panel) of the resolved clouds of NGC 5064. The solid black lines show the 1 : 1 relations.

boundaries of each box; $IQR \equiv Q_3 - Q_1$, where $Q_1$ and $Q_3$ are the first and third quartiles of the distribution of each quantity), median (thick horizontal line), and lower and upper limits (upper and lower whiskers). The retrograde clouds are on average $\approx 18$ per cent larger, $\approx 58$ per cent more massive, $\approx 15$ per cent more turbulent and have $\approx 17$ per cent larger gas mass surface densities than the prograde clouds. This suggests that the mechanism producing retrograde clouds may also have important effects on cloud properties, i.e. while the clouds become retrograde they also become larger, more massive, more turbulent and denser. Potential mechanisms are discussed in Section 6.1.

### 5.3 Velocity gradient origin

We now investigate the origin of the observed velocity gradients in the clouds of NGC 5064. The velocities we observe in the clouds result from a combination of the projected galaxy rotation and the clouds' own motions, such as intrinsic rotation and/or turbulence. Therefore, the observed velocity gradients of clouds is mainly a consequence of (i) the 'projection' of galaxy rotation (Utomo et al. 2015; Liu et al. 2021), (ii) the clouds' own intrinsic rotation driven by large-scale collapse (with angular velocities inherited from the surrounding gas; Braine et al. 2018, 2020) and/or (iii) the turbulent velocity field (Burkert & Bodenheimer 2000). We discuss each of these mechanisms in more detail in turn below.

#### *5.3.1 'Projection' of galaxy rotation*

Large-scale galaxy rotation can give rise to 'apparent' rotation in clouds. This projection effect is often observed in the molecular clouds located at the centres of early-type galaxies, where external gravitational forces are significant (Utomo et al. 2015; Liu et al. 2021). In such cases, the observed cloud rotation largely mirrors the galaxy's overall rotation, rather than reflecting the intrinsic rotation of the clouds themselves. The rotational axes and angular velocities of the clouds are expected to align with those of the galaxy at their respective locations. As shown in Fig. 11, there is no trend for the (projected) angular momenta of the NGC 5064 clouds to be tangential to the large-scale isovelocity contours, suggesting that the velocity gradients of the clouds are not due to the large-scale galaxy rotation. This is similar to the results for the clouds of the MW (Koda et al. 2006) and M 31 (Rosolowsky 2007), for which the rotational axes are randomly distributed, but it is different from the results for the clouds of the early-type galaxies NGC 4526 (Utomo et al. 2015) and NGC 4429 (Liu et al. 2021), for which the rotational axes are strongly aligned with the large-scale isovelocity contours.

To further quantify to what extent the large-scale galaxy rotation could contribute to the observed velocity gradients, we compare in Fig. 14 the measured angular velocities $\omega_{obs}$ and rotation axes $\phi_{rot}$ of the clouds to those expected from pure galaxy rotation ($\omega_{model}$ and $\phi_{model}$; calculated over the same area as each cloud and using the same method described in Section 5.1). The model overestimates the observed velocity gradients by a median factor of 3.7. In addition, the position angles of the rotation axes predicted by the model are totally uncorrelated with the observed ones (i.e. they do not follow the otherwise expected 1 : 1 correlation; see the right panel of Fig. 14). In fact, as mentioned in Section 5.2, $\approx 67$ per cent of the resolved clouds rotate internally in a direction opposite to that of the large-scale galaxy rotation. Figs 11 and 14 thus clearly suggest that processes other than galaxy rotation dominate the observed internal velocity gradients of the clouds of NGC 5064.

#### *5.3.2 Intrinsic cloud rotation driven by large-scale collapse*

If clouds are rotating and inherited their angular velocities from the surrounding gas at formation, velocity gradients across the clouds are also expected. In this scenario, where external gravitational forces are negligible, clouds form through the condensation of large-scale, rotating gas via gravitational collapse, developing intrinsic, self-gravity-driven rotation. While the angular momentum vector of an individual cloud can be somewhat misaligned with respect to that of the large-scale galaxy rotation, the average angular momentum of a large number of clouds will necessarily be prograde (Imara & Blitz 2011; Imara et al. 2011a; Williamson et al. 2014; Braine et al. 2018, 2020). Consequently, most clouds should have prograde rotational axes (although not necessarily completely aligned with the direction of galaxy rotation), and their angular velocities should be larger than that of the surrounding gas (or galaxy rotation) due to

conservation of angular momentum (Imara & Blitz 2011; Imara et al. 2011b).

Contrary to the expectations of this simple cloud formation scenario, the NGC 5064 clouds have their (projected) rotational axes in a direction primarily opposite that of the galaxy rotation (see Fig. 11 and the right panel of Fig. 14). The clouds also have angular velocities smaller than those expected from galaxy rotation (see the left panel of Fig. 14). It is thus unlikely that the NGC 5064 cloud velocity gradients are due to ordered intrinsic cloud rotation inherited during cloud formation.

#### 5.3.3 Turbulence

Another mechanism potentially able to produce (projected) linear velocity gradients, i.e. 'apparent' rotation, across clouds is turbulence. Simulations show that, even if the motions within clouds are completely random, systematic velocity gradients (that can easily be interpreted as solid-body rotation) can still arise in many clouds (Burkert & Bodenheimer 2000; Chen & Ostriker 2018; Gaudel et al. 2020). Burkert & Bodenheimer (2000) suggested that the assumption of rigid body rotation provides a good estimate of the intrinsic angular momenta of a large sample of turbulent clouds (rather than for an individual cloud). On a statistical basis, velocity gradients produced by turbulence exhibit a form (Burkert & Bodenheimer 2000)

$$\left(\frac{\omega_{\rm turb}}{\rm km\ s^{-1}\ pc^{-1}}\right) = 0.50 \left(\frac{R_{\rm c}}{1\ \rm pc}\right)^{-\frac{1}{2}} . \quad (8)$$

Taking $R_{\rm c} = 50$ pc (the most probable cloud radius of NGC 5064; see Section 3.2) yields $\omega_{\rm turb} \approx 0.07\ \rm km\ s^{-1}\ pc^{-1}$, exactly the average (and also the most probable) velocity gradient measured in NGC 5064.

Another way to assess whether the observed velocity gradients of clouds are dominated by turbulent motions is to examine the dependency of the cloud specific angular momenta

$$j_{\rm obs} \propto v_{\rm rot} R_{\rm c} \quad (9)$$

on the cloud radii $R_{\rm c}$ (Goodman et al. 1993; Pirogov et al. 2003; Tatematsu et al. 2016; Chen & Ostriker 2018), where $v_{\rm rot}$ is the internal rotational velocity of each cloud measured at $R_{\rm c}$. If the specific angular momenta of the clouds are set by turbulent velocities, we expect

$$j_{\rm obs}^{\rm turb} \propto v_{\rm rot} R_{\rm c} \propto \sigma_{\rm obs,los} R_{\rm c} \propto R_{\rm c}^{1.6} \quad (10)$$

using our measured size–linewidth relation ($\sigma_{\rm obs,los} \propto R_{\rm c}^{0.6}$; equation 3). Here we have used $v_{\rm rot} \propto \sigma_{\rm obs,los}$ assuming solid-body rotation with an angular velocity $\omega_{\rm rot}$. In this case, the observed line-of-sight velocity dispersion $\sigma_{\rm obs,los}$ can be approximated as $\sigma^2_{\rm obs,los} \propto \omega^2_{\rm rot} R_{\rm c}^2 \sin^2 i \approx v^2_{\rm rot}(R_{\rm c}) \sin^2 i$ (see equations B10 and B23 of Liu et al. 2021), where $i$ is the inclination angle of the given cloud along the line of sight. Fig. 15 shows the specific angular momenta of the NGC 5064 clouds $j_{\rm obs}$ as a function of their radii $R_{\rm c}$. The best-fitting power law is $j_{\rm obs} \propto R_{\rm c}^{1.90\pm0.32}$, shown as a solid line in Fig. 15, in broad agreement with the relation expected above (equation 10).

Overall, the observed (projected) angular momenta of the clouds of NGC 5064 are poorly fitted by models that assume the bulk internal motions of clouds are purely due to (1) the projection of the large-scale galaxy rotation and (2) angular velocities inherited from the surrounding gas at formation. Conversely, the average velocity gradient and the $j_{\rm obs} - R_{\rm c}$ relation of the NGC 5064 clouds are consistent with the expectations from turbulence. These results suggest that the velocity gradients of the NGC 5064 clouds are largely independent of the galaxy rotation and arise primarily from random turbulent motions. Thus, the observed rotation of the NGC 5064 clouds is only 'apparent' nature, as opposed to genuine internal bulk rotation.

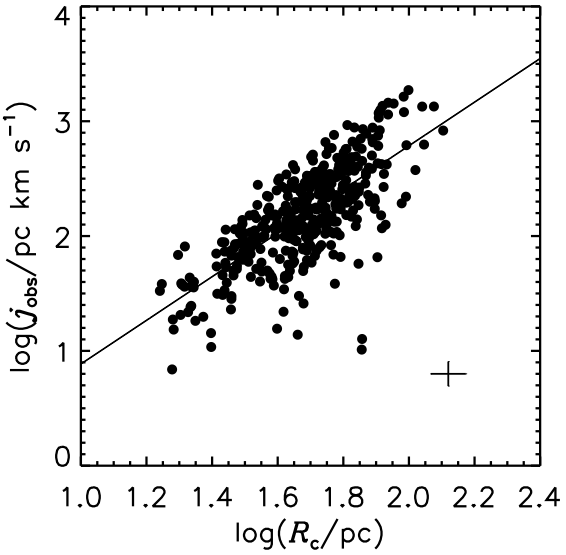


**Figure 15.** Specific angular momenta $j_{\rm obs}$ of the resolved NGC 5064 clouds as a function of their sizes $R_{\rm c}$. The typical uncertainty is shown as a cross in the bottom-right corner. The best-fitting power law $j_{\rm obs} \propto R_{\rm c}^{1.90\pm0.32}$ is shown as a solid line.

## 6 DISCUSSION

### 6.1 High fraction of retrograde clouds

We found a major population of clouds that internally rotate in a direction opposite to the large-scale galaxy rotation ($f_{\rm retro} \approx 67$ per cent; see Section 5.2). What mechanisms could produce this unusually high retrograde fraction? Simulations show that retrograde clouds form through several physical processes: (1) large-scale perturbations such as shocks in a bar region (bar-induced shocks; Tasker & Tan 2009; section 3.2.1 of Fujimoto, Tasker & Habe 2014) and spiral arms (spiral shocks; Chernin & Efremov 1995; Dobbs, Burkert & Pringle 2011; Fujimoto et al. 2014; Braine et al. 2020), (2) stellar feedback (Dobbs et al. 2011, 2014; Williamson et al. 2014), and (3) cloud–cloud collisions (Dobbs 2008, 2015; Tasker & Tan 2009; Dobbs et al. 2011; Benincasa et al. 2013; Dobbs & Pringle 2013; Li et al. 2018). It is worth noting that while these mechanisms can generate random velocity gradients, they are not expected to systematically prefer retrograde rotation. In addition to these physical mechanisms, projection effects associated with NGC 5064's high-inclination angle, may further enhance the 'apparent' retrograde fraction. We discuss each of these factors in turn below.

#### 6.1.1 Galactic shocks in the bar region and spiral arms

Simulations and observations have shown that the fraction of retrograde clouds is highest in bars – though prograde clouds still dominate (Fujimoto et al. 2014) – followed by spiral arms (Chernin & Efremov 1995; Dobbs et al. 2011; Fujimoto et al. 2014; Braine et al. 2020). In the remaining disc regions, clouds are predominantly prograde. As shown in Figs 2 and 4, the $^{12}$CO(2–1) maps do not show

any evidence of a galactic bar or spiral pattern in the central regions of NGC 5064. Furthermore, this galaxy displays a high degree of flocculence in its optical imagery captured by the *HST*, lacking well-defined bars or spiral arms (Funes et al. 2002; Davis et al. 2022). It is thus unlikely that the high fraction of retrograde clouds in NGC 5064 is caused by large-scale shocks.

### 6.1.2 *Stellar feedback*

Another important mechanism to produce retrograde clouds is stellar feedback. Simulations have shown that stellar feedback contributes to the turbulence that can stir up clouds, leading to a population of clouds with retrograde internal rotation (Dobbs et al. 2011; Williamson et al. 2014; Dobbs 2015). In simulations, greater star formation leads to a larger fraction of retrograde clouds, and this fraction (induced by stellar feedback) can reach 40–60 per cent (Dobbs et al. 2014; Williamson et al. 2014; Dobbs 2015). The simulations further suggest that, if stellar feedback is the source of retrograde clouds, the proportion of small, low-mass clouds exhibiting retrograde motion should exceed that of large, high-mass clouds (e.g. Dobbs et al. 2011; Williamson et al. 2014). This is because small low-mass cloud are more strongly influenced by stellar feedback, and are thus more likely to become retrograde, while large high-mass clouds have angular momenta that tend to approach that of the galaxy, and are thus more likely to be prograde (Williamson et al. 2014).

However, in NGC 5064, the retrograde clouds are larger and more massive than the prograde clouds (see Section 5.2), in contrast to the simulation results (e.g. Dobbs et al. 2011; Williamson et al. 2014). Stellar feedback is thus again unlikely to be the dominant mechanism at the origin of the turbulence and thus the retrograde clouds of NGC 5064.

### 6.1.3 *Cloud–cloud collisions*

Cloud–cloud collision can be another important mechanism to produce retrograde clouds. If clouds form predominantly by collisional build-up of smaller structures, the fraction of retrograde clouds can be significantly increased (Dobbs 2008, 2015; Tasker & Tan 2009; Dobbs et al. 2011; Benincasa et al. 2013; Dobbs & Pringle 2013; Li et al. 2018). Numerical simulations suggest that, without a bar and/or spiral potential and stellar feedback, clouds can only become retrograde through collisions (Dobbs et al. 2011; Williamson et al. 2014), and large $f_{\rm retro}$ may indicate that clouds have evolved collisionally (Li et al. 2018). In simulations focused on cloud–cloud collisions, approximately $40-50$ per cent of the resulting clouds exhibit retrograde rotation (Tasker & Tan 2009; Dobbs et al. 2011; Benincasa et al. 2013).

Cloud–cloud collisions can lead to the formation of larger, more massive clouds through repeated interactions and mergers. These processes are known to randomize the angular momentum of the resulting structures and, in some cases, can invert the direction of internal rotation relative to the galaxy's large-scale motion. While these mechanisms are not expected to preferentially produce retrograde rotation, they can contribute to a diverse distribution of spin orientations. This may help explain the elevated retrograde fraction observed in NGC5064, where retrograde clouds are systematically larger and more massive than their prograde counterparts (see Section 5.2).

Additional evidence for the importance of cloud–cloud collisions in NGC 5064 comes from the structure of its gas disc, which is clumpy and gravitationally unstable ($Q \approx 1$; see Fig. 16). Simulations (e.g. Dobbs & Bonnell 2006; Dobbs 2008) and observations (e.g. Liu et al. 2022) both suggest that collisions play a particularly important role in clumpy, gravitationally unstable discs. In this context, galactic shear drives frequent cloud–cloud interactions, with collision time-scales significantly shorter than traditional estimates–on the order of ∼1/5 of the orbital period, rather than hundreds of Myr (Tasker & Tan 2009). The clumpy, unstable nature of the disc also suggests that collisions contribute to maintaining the observed turbulence, as they are a key driver of turbulent motions in these settings (e.g. Liu et al. 2022). This collision-driven turbulence can disrupt the internal motions of clouds, causing them to lose memory of the galaxy's large-scale rotation and leading to the formation of a larger retrograde cloud population (e.g. Tasker & Tan 2009; Dobbs 2015; Li et al. 2018). Thus, the high frequency of retrograde clouds may itself be a diagnostic of a clumpy, collision-rich ISM (Dobbs 2008). To test this scenario, higher-resolution observations of molecular gas will be essential–particularly at spatial scales comparable to the critical collision length, $\lambda_{\rm coll} = G\Sigma_{\rm gas,disc}/2A^2$, where $\Sigma_{\rm gas,disc}$ is the gas surface density and $A$ is Oort's constant (Liu et al. 2022).

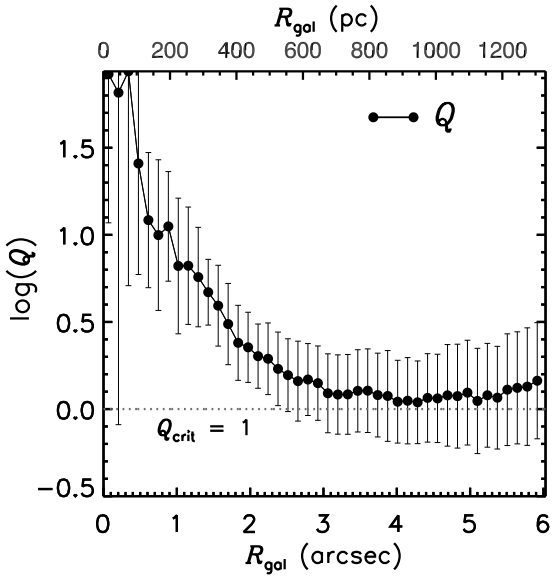


**Figure 16.** Radial variation of the Toomre parameter $Q$ of NGC 5064, averaged over elliptical annuli of width 30 pc. The Toomre parameter $Q \gg 1$ in the central regions but drops to $\approx 1$ at large radii. The grey dotted horizontal line indicates $Q = Q_{\rm crit} = 1$.

### 6.1.4 *Projection effects (observational bias)*

Cloud–cloud collisions appear to be the primary physical mechanism producing retrograde clouds in NGC 5064; however, this process alone does not fully explain the unusually high observed retrograde fraction of $f_{\rm retro} \approx 67$ per cent. This value exceeds the retrograde fractions of $f_{\rm retro} \approx 40$–$50$ per cent reported in simulations of cloud–cloud collisions (Tasker & Tan 2009; Dobbs et al. 2011; Benincasa et al. 2013). Therefore, in addition to physical mechanisms, observational biases may also contribute to the elevated retrograde fraction. A likely source of such bias is projection effects. Simulations by Tasker & Tan (2009) indicate that the measured retrograde fraction is sensitive to the inclination angle of the galaxy. For example, in edge-on configurations ($i = 90°$), projection effects can cause the observed

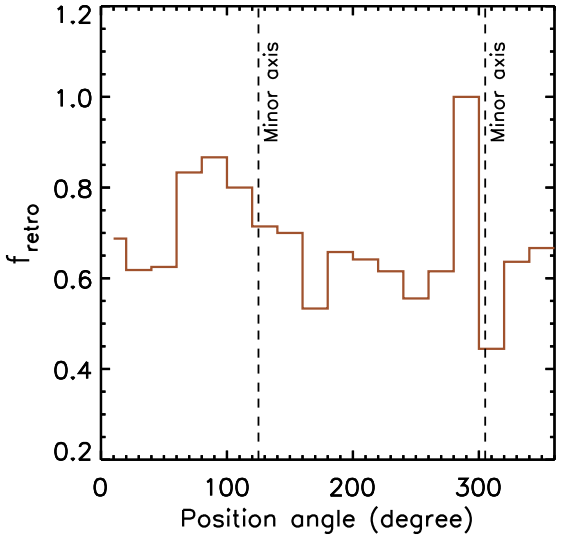


**Figure 17.** Retrograde cloud fraction $f_{retro}$ as a function of azimuthal angle in NGC 5064. Vertical dashed lines indicate the directions of the galaxy's minor axis.

retrograde fraction to be nearly twice the intrinsic value. Given the high inclination angle of NGC 5064 ($i = 70.^{\circ}8$) and the use of only line-of-sight velocities to infer cloud rotation, projection effects are likely contributing to the elevated retrograde fraction observed in this galaxy.

If projection effects are significant, one would expect the apparent retrograde fraction to be higher along the direction of the minor axis. This is because, along the minor axis, the line-of-sight component of a cloud's prograde rotation – aligned with the galaxy's overall rotation – is minimized. As a result, the observable signature of prograde rotation can be suppressed, while internal cloud motions – such as turbulence or vertical flows – become more prominent and may mimic retrograde rotation. In addition, clouds near the minor axis are more likely to overlap along the line of sight, leading to velocity blending that further increases the likelihood of misclassifying prograde clouds as retrograde. These combined effects can artificially boost the observed retrograde fraction near the minor axis in highly inclined systems like NGC 5064.

Fig. 17 shows the distribution of retrograde cloud fractions as a function of azimuthal angle in NGC 5064, with the two vertical dashed lines indicating the directions of the galaxy's minor axis. As expected, we find an elevated retrograde fraction near the minor axis, consistent with projection effects contributing to the high-observed retrograde fraction.

However, while projection effects likely amplify the observed retrograde fraction, they cannot fully account for the high fraction of retrograde clouds. As shown in Fig. 17, the retrograde fraction remains substantial even along the major axis, where projection effects should be minimal. Moreover, in another WISDOM galaxy–NGC4429 – which is also highly inclined (inclination angle of 68°), the cloud population is entirely dominated by prograde rotation (Liu et al. 2021). This suggests that a high inclination angle alone does not necessarily result in a high retrograde fraction. Although it remains uncertain whether the *true* retrograde fraction is statistically significantly higher than $\sim 50$ per cent, NGC 5064 likely hosts an intrinsically high retrograde fraction, driven by the physical mechanisms such as cloud–cloud collisions discussed above, with projection effects further boosting the observed value. Further investigation into the role of projection effects is needed to better quantify their impact on measurements of retrograde cloud rotation.

In summary, we investigated several physical mechanisms that could account for the high-retrograde fraction observed in NGC 5064 ($f_{retro} \approx 67$ per cent). Large-scale galactic shocks are unlikely to be responsible, as NGC 5064 lacks a bar or spiral structure. Stellar feedback is also unlikely to be the dominant mechanism, since retrograde clouds in NGC 5064 are larger and more massive than prograde ones, contrary to simulation predictions. Instead, cloud–cloud collisions seem to provide the most consistent explanation, supported by the observation that retrograde clouds are systematically larger and more massive than their prograde counterparts, and by the clumpy, gravitationally unstable nature of the galaxy's gas disc. However, further investigation into the role of cloud–cloud collisions is required to confirm this scenario. Additionally, projection effects due to the galaxy's high inclination may further amplify the observed retrograde fraction, making it appear even higher than the already elevated intrinsic value.

### 6.2 Effects of external gravity

We now assess the impact of external gravity, i.e. shear and tidal forces, on the clouds of NGC 5064. The very high fraction of retrograde clouds ($f_{retro} \approx 67$ per cent; see Section 5.2) suggests that external gravity is not important, as otherwise the clouds would be mostly prograde (Williamson et al. 2014; Utomo et al. 2015; Liu et al. 2021). To confirm this speculation, we now compare (i) the cloud sizes $R_c$ to their tidal radii $R_t$ and (ii) the contribution of external gravity to a cloud's energy budget ($E_{ext}$) to the self-gravitational energy of the cloud ($U_{sg}$).

A common way to assess the importance of external gravity compared to self-gravity is to compare the tidal radius of a cloud to is size. Following Liu et al. (2021), we adopt the tidal radius $R_t$ defined by Gammie, Ostriker & Jog (1991) and Tan (2000),

$$R_t \equiv \left(\frac{G}{2A^2}\right)^{1/3} M_{gas}^{1/3} , \tag{11}$$

where $A$ is the Oort constant and $M_{gas}$ is the gas mass of the cloud. Here, a spherical galaxy mass distribution has been assumed. The tidal radius defined in this manner represents the maximum size of a gravitationally bound cloud (of a given mass $M_{gas}$) allowed by the galaxy rotational shear (quantified by the Oort constant $A$). This definition of the tidal radius also denotes the distance where the contribution of external gravity to a cloud's energy budget is equal to the cloud's self-gravitational energy (if the gas exactly follows the galaxy rotation within the cloud; Liu et al. 2021).

Fig. 18 shows the comparison of the sizes $R_c$ and tidal radii $R_t$ of the resolved clouds of NGC 5064. Overall, $\approx 94$ per cent (362/387) of the resolved clouds of NGC 5064 have sizes smaller than their tidal radii, with a mean ratio $\langle R_c/R_t \rangle = 0.61$. This appears to confirm that external gravity can not be important to the clouds of NGC 5064.

To further quantify the influence of external gravity on the clouds of NGC 5064, we calculate the contribution of external gravity to each clouds' energy budget $E_{ext}$ following equation 28 of Liu et al. (2021):

$$E_{ext} = M_{gas} \left(\sigma_{gal,r}^2 + \sigma_{gal,t}^2 + b_e(T_0 - 2\Omega_0^2)R_c^2\right) , \tag{12}$$

where $\sigma_{gal,r}$ and $\sigma_{gal,t}$ are the RMS velocity of gas motions due to external gravity in the radial and the azimuthal direction, respectively, $b_e$ a geometrical factor that quantifies the effects of inhomogeneities

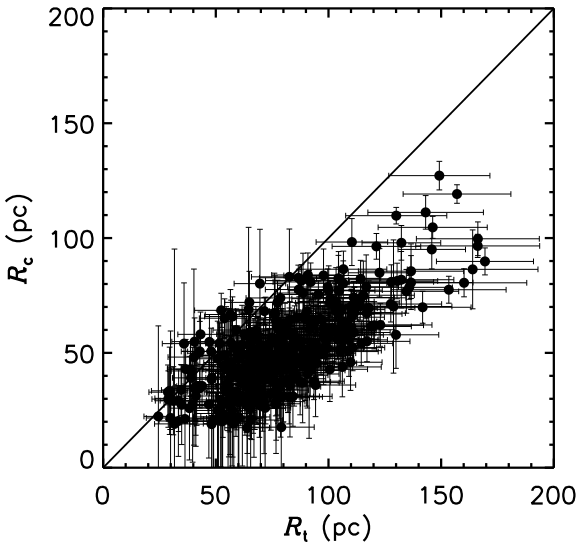


**Figure 18.** Comparison of the sizes and tidal radii of the resolved clouds of NGC 5064. The black solid diagonal line shows the 1 : 1 relation.

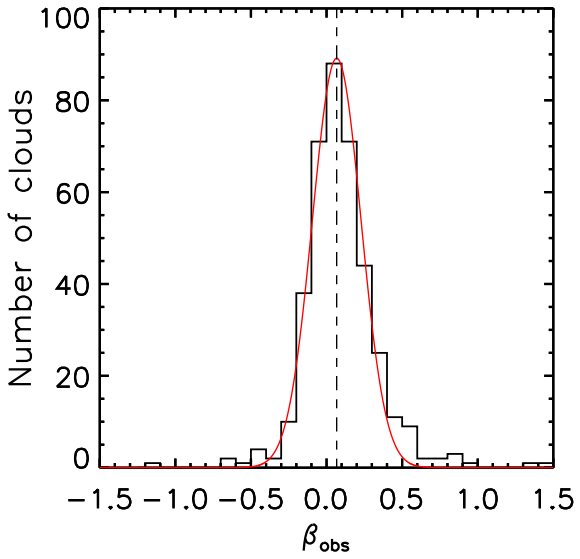


**Figure 19.** Distribution of $\beta_{obs}$, defined as the ratio of the contribution of external gravity to a cloud's energy budget $E_{ext}$ and the (absolute value of the) cloud's self-gravitational energy $U_{sg}$. The black dashed vertical line shows the mean of a Gaussian fit (red solid line) to the distribution.

associated with external gravity ($b_e = 1/5$ for a spherical homogeneous cloud), $\Omega_0$ the circular orbital angular velocity of the galaxy at the cloud's centre, and $T_0$ the tidal acceleration per unit length in the radial direction evaluated at the cloud's centre (both calculated using the previously-derived circular velocity curve; see Fig. 12). We note that equation (12) assumes the cloud is in vertical equilibrium, meaning that the contribution of the external gravity to the cloud's energy budget (i.e. the sum of gravitational energy from external gravity and the cloud's kinetic energy) in the vertical direction vanishes.

The RMS velocities of gas motions due to external gravity $\sigma_{gal,r}$ and $\sigma_{gal,t}$ can be calculated from equation 29 of Liu et al. (2021):

$$\sigma_{gal,r} = \sigma_{gal,t} \approx \frac{\sigma^2_{obs,los} - \sigma^2_{gs,los}}{\sin^2 i} \ , \tag{13}$$

where $\sigma_{obs,los}$ and $\sigma_{gs,los}$ are the observed and the gradient-subtracted velocity dispersion, respectively, and $i = 70.^\circ8$ is the inclination angle of the galaxy. Equation (13) is derived by assuming the gas motions due to external gravity are isotropic in the plane (i.e. $\sigma_{gal,r} = \sigma_{gal,t}$; see Liu et al. 2021). Here, we make use of the gradient-subtracted velocity dispersion $\sigma_{gs,los}$ of each cloud of NGC 5064, obtained by subtracting the contribution of bulk motions to the observed velocity dispersion $\sigma_{obs,los}$ (see Utomo et al. 2015; Liu et al. 2021), that is also listed in Table 1. It turns out that $\sigma_{gs,los}$ is not significantly different from $\sigma_{obs,los}$ for most of the clouds of NGC 5064, with a mean difference $\langle \sigma_{obs,los} - \sigma_{gs,los} \rangle = 1.6$ km s$^{-1}$, $\approx 30$ per cent of the mean of $\sigma_{obs,los}$ (i.e. $\langle \frac{\sigma_{gs,los}}{\sigma_{obs,los}} \rangle \approx 0.7$). This is consistent with our earlier finding that the dynamics of the NGC 5064 clouds is generally decoupled from the large-scale galaxy rotation (Section 5.3).

We can now calculate the ratio between the contribution of external gravity to a cloud's energy budget ($E_{ext}$) and the cloud's self-gravitational energy ($U_{sg}$):

$$\beta_{obs} \equiv \frac{E_{ext}}{|U_{sg}|} \ , \tag{14}$$

where $U_{sg} = -\frac{3}{5}\frac{GM^2_{gas}}{R_c}$ (again assuming a spherical homogeneous cloud). Fig. 19 shows the distribution of $\beta_{obs}$ for the resolved clouds of NGC 5064. Almost all resolved clouds have $\beta_{obs} < 1$, and a Gaussian fit to the distributions yields a mean $\langle \beta_{obs} \rangle = 0.07 \pm 0.01$. The very small $\beta_{obs}$ again suggest that external gravity is not important for the NGC 5064 clouds.

Interestingly, $\approx 1/3$ (129/387) of the resolved clouds of NGC 5064 have a negative energy contribution from external gravity, i.e. $E_{ext} < 0$. This suggests that, instead of supporting the clouds against self-gravity, external gravity actually contributes to the gravitational bounding of the clouds. Such negative $E_{ext}$ can arise because (i) gas motions due to external gravity (i.e. large-scale galaxy rotation) are negligible in some clouds (i.e. $\sigma_{gal,r} \approx \sigma_{gal,t} \approx 0$ as $\sigma_{obs,los} \approx \sigma_{gs,los}$) and (ii) $(T_0 - 2\Omega_0^2)R_c^2 \lesssim 0$ at most galactocentric radii (see Fig. 12). A negative contribution of external gravity to a cloud's energy budget has also been observed in simulations of a MW-type galaxy (Ramírez-Galeano et al. 2022). Nevertheless, as the majority ($\approx 2/3$) of the resolved clouds of NGC 5064 have $E_{ext} > 0$, external gravity generally supports the clouds against self-gravity, even though the energy contributed is almost negligible.

Finally, we calculate the ratio between the contribution of external gravity to a cloud's energy budget ($E_{ext}$) and the cloud's turbulent energy ($K_{turb}$):

$$\gamma_{obs} \equiv \frac{E_{ext}}{K_{turb}} = \frac{E_{ext}}{\frac{3}{2}M_{gas}\sigma^2_{obs,los}} \ . \tag{15}$$

Fig. 20 shows the distribution of $\gamma_{obs}$ for the resolved clouds of NGC 5064. A Gaussian fit to the distribution yields a mean $\langle \gamma_{obs} \rangle = 0.41 \pm 0.02$. About 95 per cent (368/387) of the resolved clouds of NGC 5064 have $\gamma_{obs} \leq 1$. Thus, external gravity is less important than turbulence, that in turn is less important than self-gravity, i.e. $\langle \alpha_{obs,vir} \rangle \equiv \langle M_{obs,vir}/M_{gas} \rangle = \langle 2K_{turb}/U_{sg} \rangle = 0.48 \pm 0.03$ (see Section 4.2). It thus appears that self-gravity and turbulence are the two dominant factors regulating the clouds of NGC 5064, while external gravity can be ignored.

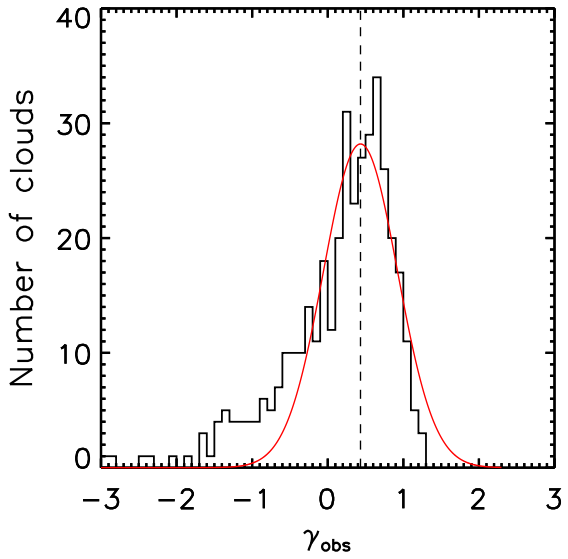


**Figure 20.** Distribution of $\gamma_{obs}$, defined as the ratio of the contribution of the external potential to a cloud's energy budget $E_{ext}$ and the cloud's turbulent energy $K_{turb}$. The black dashed vertical line shows the mean of a Gaussian fit (red solid line) to the distribution.

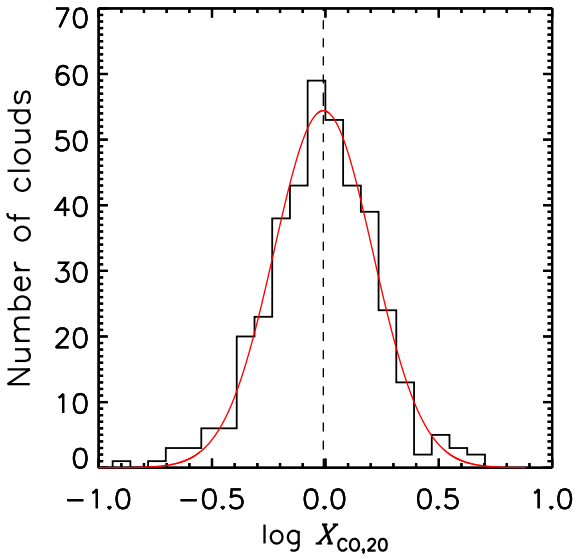


**Figure 21.** Distribution of $X_{CO,20}$ of the resolved clouds of NGC 5064 (black histogram), inferred by assuming each cloud is in virial equilibrium. The black dashed line shows the most probable $X_{CO,20}$. A lognormal fit (red solid curve) to the distribution yields a mean $\langle \log(X_{CO,20}) \rangle = -0.065 \pm 0.012$.

### 6.3 Low virial parameters or low CO conversion factors?

In Section 4.2, we determined that the clouds of NGC 5064 have relatively small virial parameters ($\langle \alpha_{obs,vir} \rangle = 0.48 \pm 0.03$). These small virial parameters imply either that (i) the clouds are strongly self-gravitating or (ii) the clouds are virialized but their CO conversion factors are smaller than the assumed standard Galactic factor ($X_{CO} = 2 \times 10^{20}$ cm$^{-2}$ (K km s$^{-1}$)$^{-1}$). We examine both scenarios below.

If the measured low virial parameters reflect the true dynamical state of the clouds, this implies that turbulence alone is insufficient to support them against gravitational collapse. This scenario is physically plausible in the context of NGC 5064, which hosts a gravitationally unstable gas disc ($Q \approx 1$; see Fig. 16). It is also consistent with simulations and theoretical studies suggesting that, in such unstable discs, local gas can undergo rapid collapse and fragmentation on cloud scales (e.g. Bournaud & Elmegreen 2009; Krumholz & Dekel 2010; Hopkins et al. 2012). In this regime, self-gravity dominates over turbulent and rotational support, naturally resulting in clouds with low virial parameters. It is also possible, however, that additional support mechanisms – such as strong magnetic fields – may play a role in counteracting gravitational collapse.

Alternatively, the low virial parameters could result from an overestimate of the cloud masses due to the assumption of a standard CO-to-$H_2$ conversion factor ($X_{CO} = 2 \times 10^{20}$ cm$^{-2}$ (K km s$^{-1}$)$^{-1}$). If we instead assume that the clouds of NGC 5064 are in virial equilibria (i.e. that $\alpha_{obs,vir} = 1$), we can turn the problem around and derive an estimate of $X_{CO}$ for each resolved cloud of NGC 5064. For convenience, we define

$$X_{CO,20} \equiv \frac{X_{CO}}{1 \times 10^{20}\ \mathrm{cm^{-2}}\ (\mathrm{K\ km\ s^{-1}})^{-1}}. \quad (16)$$

The distribution of these inferred $X_{CO,20}$, assuming the resolved clouds of NGC 5064 are in virial equilibria, is shown in Fig. 21. A lognormal fit to the distribution yields a best-fitting median $X_{CO,20} = 0.96 \pm 0.02$. This is smaller than but within a factor of $\approx 2$ of the standard Galactic conversion factor ($X_{CO,20} = 2$). It aligns closely with the conversion factors derived for the clouds of NGC 6946 ($X_{CO,20} \approx 1.2$; Donovan Meyer et al. 2013) and NGC 4826 ($X_{CO,20} \approx 1.27$; Donovan Meyer et al. 2013), but it is slightly smaller than those of the clouds of NGC 4736 ($X_{CO,20} \approx 1.83$; Donovan Meyer et al. 2013). The methodology employed by Donovan Meyer et al. (2013) to derive $X_{CO,20}$ is the same one used here (i.e. it assumes the clouds are in virial equilibria).

An explanation for the putative smaller $X_{CO}$ of NGC 5064 is however required. Observations and simulations have established that $X_{CO}$ depends on the local properties of the ISM (e.g. Kutner & Leung 1985; Elmegreen 1989; Bell et al. 2006). Previous studies have found $X_{CO}$ in the central regions of some spiral galaxies to be as much as one order of magnitude smaller than the standard Galactic conversion factor (e.g. Israel & Baas 2001, 2003). For example, Israel, Tilanus & Baas (2006) found $X_{CO}$ in the central regions of the spiral galaxy M 51 to be 4 to 5 times smaller than the standard Galactic conversion factor, while Sodroski et al. (1995) inferred a conversion factor in the vicinity of the Galactic centre 3 to 10 times smaller than that in the Galactic disc. Stronger turbulence, higher molecular gas mass densities, stronger radiation fields, greater cosmic ionisation and/or higher metallicities can produce a slightly smaller $X_{CO}$ at the centres of galaxies (e.g. Bell et al. 2006; Bolatto, Wolfire & Leroy 2013).

At present, it is not possible to determine conclusively which of the two scenarios–strong self-gravity or magnetic support, versus a reduced CO-to-$H_2$ conversion factor – best explains the low-virial parameters observed in NGC 5064. Both interpretations are physically plausible in the context of this galaxy. To distinguish between them, independent observational constraints on $X_{CO}$ are required. Such measurements would enable more accurate determinations of cloud masses and dynamical states, and are essential for resolving the origin of the low virial parameters in this system.

## 7 CONCLUSIONS

We presented high-resolution (0.14 arcsec × 0.12 arcsec or 31 × 25 $pc^2$) ALMA $^{12}CO(J = 2–1)$ observations of the spiral galaxy NGC 5064. We identified 478 molecular clouds, of which 387 are spatially and spectrally resolved. We report the following conclusions:

(i) The clouds of NGC 5064 have similar sizes (17–127 pc), molecular gas masses ($2.5 \times 10^5$–$3.2 \times 10^7$ $M_\odot$) and velocity dispersions (1.2–15.9 km $s^{-1}$) as those of the Milky Way and Local Group galaxies. However, they possess slightly larger molecular gas mass surface densities (95–$2.0 \times 10^3$ $M_\odot$ $pc^{-2}$).

(ii) The radial distributions of cloud size, gas mass, velocity dispersion and gas mass surface density exhibit a peak at $R_{gal} \approx 500$ pc, within which a central CO depression has been observed. Beyond this peak, all cloud properties exhibit a slight decrease with increasing galactocentric distance.

(iii) The cloud cumulative gas mass function follows a truncated power law with a best-fitting index $\gamma = -1.92 \pm 0.07$ and a truncation mass of $2.93 \pm 0.39 \times 10^7$ $M_\odot$.

(iv) The Larson relations for the clouds of NGC 5064 are comparable to those of the Milky Way disc and Local Group galaxy clouds. Specifically, $\sigma_{obs,los} \propto R_c^{0.6\pm0.1}$, $L_{CO(2-1)} \propto R_c^{2.8\pm0.1}$, and $L_{CO(2-1)} \propto \sigma_{obs,los}^{2.5\pm0.2}$.

(v) The measured virial parameters indicate that the clouds of NGC 5064 are strongly gravitationally bound or magnetic support, with a low average $\langle\alpha_{obs,vir}\rangle = 0.48 \pm 0.03$. Alternatively, if the clouds are assumed to be virialized, their $X_{CO}$ factors may be lower than the standard Galactic conversion factor ($X_{CO} = 0.96 \pm 0.02 \times 10^{20}$ $cm^{-2}$ (K km $s^{-1})^{-1}$).

(vi) The velocity gradients of the clouds, ranging from 0.01 to 0.23 km $s^{-1}$ $pc^{-1}$, are comparable to those observed in the clouds of Milky Way, M 31 and M 33. These gradients appear to arise from turbulence rather than the large-scale galaxy rotation or cloud's intrinsic rotation.

(vii) A high fraction (257/387 or 67 per cent) of the clouds exhibit retrograde internal rotation. These retrograde clouds have on average 18 per cent larger sizes, 58 per cent larger masses, 15 per cent increased turbulence and 17 per cent larger gas mass surface densities than prograde clouds.

Cloud–cloud collisions provide the most consistent physical explanation for the high-retrograde fraction observed in NGC 5064, though further investigation is needed to confirm this scenario. Projection effects due to the galaxy's high inclination may further enhance the apparent retrograde fraction, contributing to the unusually high observed value that exceeds 50 per cent. Confirmation using less inclined systems is essential to determine whether the observed dominance of retrograde rotation reflects an intrinsic physical property or is primarily shaped by projection effects.

(viii) External gravity (e.g. shear and tidal forces) does not appear to play a significant role in shaping the clouds of NGC 5064.

## DATA AVALABILITY

The data underlying this article are available in the ALMA archive (https://almascience.eso.org/asax/) under project code: (i) 2015.1.00466.S and (ii) 2016.2.00053.S. This publication is based on data acquired with the Atacama Pathfinder Experiment (APEX) under programme ID [O-093.F-9309A]. APEX is a collaboration between the Max-Planck-Institut fur Radioastronomie, the European Southern Observatory, and the Onsala Space Observatory. Swedish observations on APEX are supported through Swedish Research Council grant No 2017–00648.

## ACKNOWLEDGEMENTS

We thank the Referee for their valuable comments and suggestions, which have helped improve the clarity and quality of the paper. LL was supported by a DAWN Fellowship, funded by the Danish National Research Foundation under grant No. 140. MB was supported by STFC consolidated grant 'Astrophysics at Oxford' ST/K00106X/1 and ST/W000903/1.

This paper makes use of ALMA data. ALMA is a partnership of ESO (representing its member states), NSF (USA) and NINS (Japan), together with NRC (Canada) and NSC and ASIAA (Taiwan) and KASI (Republic of Korea), in cooperation with the Republic of Chile. The Joint ALMA Observatory is operated by ESO, AUI/NRAO, and NAOJ. This paper also makes use of observations made with the NASA/ESA Hubble Space Telescope, and obtained from the Hubble Legacy Archive, which is a collaboration between the Space Telescope Science Institute (STScI/NASA), the Space Telescope European Coordinating Facility (ST-ECF/ESA), and the Canadian Astronomy Data Centre (CADC/NRC/CSA). This research has made use of the NASA/IPAC Extragalactic Database (NED) which is operated by the Jet Propulsion Laboratory, California Institute of Technology, under contract with the National Aeronautics and Space Administration.

## REFERENCES

Bell T. A., Roueff E., Viti S., Williams D. A., 2006, MNRAS, 371, 1865
Benincasa S. M., Tasker E. J., Pudritz R. E., Wadsley J., 2013, ApJ, 776, 23
Bertola F., Cappellari M., Funes S. J., José G., Corsini E. M., Pizzella A., Beltrán J. C. V., 1998, ApJ, 509, L93
Bigiel F., Leroy A., Walter F., Brinks E., de Blok W. J. G., Madore B., Thornley M. D., 2008, AJ, 136, 2846
Blitz L., 1993, in Levy E. H., Lunine J. I., eds, Protostars and Planets III. p. 125
Blitz L., Fukui Y., Kawamura A., Leroy A., Mizuno N., Rosolowsky E., 2007, Protostars and Planets V. p. 81
Bolatto A. D., Leroy A. K., Rosolowsky E., Walter F., Blitz L., 2008, ApJ, 686, 948
Bolatto A. D., Wolfire M., Leroy A. K., 2013, ARA&A, 51, 207
Bournaud F., Elmegreen B. G., 2009, ApJ, 694, L158
Braine J., Rosolowsky E., Gratier P., Corbelli E., Schuster K. F., 2018, A&A, 612, A51
Braine J., Hughes A., Rosolowsky E., Gratier P., Colombo D., Meidt S., Schinnerer E., 2020, A&A, 633, A17
Burkert A., Bodenheimer P., 2000, ApJ, 543, 822
CASA Team et al., 2022, PASP, 134, 114501
Cappellari M., 2002, MNRAS, 333, 400
Cappellari M. et al., 2013, MNRAS, 432, 1709
Carilli C. L., Walter F., 2013, ARA&A, 51, 105
Chen C.-Y., Ostriker E. C., 2018, ApJ, 865, 34
Chernin A. D., Efremov Y. N., 1995, MNRAS, 275, 209
Choi W. et al., 2023, MNRAS, 522, 4078
Colombo D. et al., 2014, ApJ, 784, 3
Corbelli E. et al., 2017, A&A, 601, A146
Dame T. M., 2011, preprint (arXiv:1101.1499)
Dame T. M., Hartmann D., Thaddeus P., 2001, ApJ, 547, 792
Davis T. A. et al., 2013, MNRAS, 429, 534
Davis T. A. et al., 2018, MNRAS, 473, 3818
Davis T. A., Zabel N., Dawson J. M., 2020, Astrophysics Source Code Library, preprint (ascl:2006.003)
Davis T. A. et al., 2022, MNRAS, 512, 1522
Dobbs C. L., 2008, MNRAS, 391, 844
Dobbs C. L., 2015, MNRAS, 447, 3390
Dobbs C. L., Bonnell I. A., 2006, MNRAS, 367, 873
Dobbs C. L., Pringle J. E., 2013, MNRAS, 432, 653
Dobbs C. L., Burkert A., Pringle J. E., 2011, MNRAS, 417, 1318

Dobbs C. L. et al., 2014, in Beuther H., Klessen R. S., Dullemond C. P., Henning T., eds, Protostars and Planets VI. University of Arizona Press, Tucson, p. 3
Donovan Meyer J. et al., 2012, ApJ, 744, 42
Donovan Meyer J. et al., 2013, ApJ, 772, 107
Elmegreen B. G., 1989, ApJ, 338, 178
Faesi C. M., Lada C. J., Forbrich J., 2016, ApJ, 821, 125
Field G. B., Blackman E. G., Keto E. R., 2011, MNRAS, 416, 710
Fujimoto Y., Tasker E. J., Habe A., 2014, MNRAS, 445, L65
Fukui Y., Kawamura A., 2010, ARA&A, 48, 547
Fukui Y. et al., 2008, ApJS, 178, 56
Funes J. G., Corsini E. M., Cappellari M., Pizzella A., Vega Beltrán J. C., Scarlata C., Bertola F., 2002, A&A, 388, 50
Gammie C. F., Ostriker J. P., Jog C. J., 1991, ApJ, 378, 565
Gaudel M. et al., 2020, A&A, 637, A92
Goldreich P., Sridhar S., 1995, ApJ, 438, 763
Goodman A. A., Benson P. J., Fuller G. A., Myers P. C., 1993, ApJ, 406, 528
Gratier P. et al., 2012, A&A, 542, A108
Hernandez A. K., Tan J. C., 2015, ApJ, 809, 154
Heyer M., Krawczyk C., Duval J., Jackson J. M., 2009, ApJ, 699, 1092
Hirota A., Kuno N., Sato N., Nakanishi H., Tosaki T., Sorai K., 2011, ApJ, 737, 40
Hopkins P. F., Kereš D., Murray N., Quataert E., Hernquist L., 2012, MNRAS, 427, 968
Hughes A. et al., 2010, MNRAS, 406, 2065
Hughes A. et al., 2013, ApJ, 779, 46
Imara N., Blitz L., 2011, ApJ, 732, 78
Imara N., Bigiel F., Blitz L., 2011a, ApJ, 732, 79
Imara N., Bigiel F., Blitz L., 2011b, ApJ, 732, 79
Israel F. P., Baas F., 2001, A&A, 371, 433
Israel F. P., Baas F., 2003, A&A, 404, 495
Israel F. P., Tilanus R. P. J., Baas F., 2006, A&A, 445, 907
Kane B. D., Clemens D. P., 1997, AJ, 113, 1799
Kauffmann J., Pillai T., Zhang Q., 2013, ApJ, 765, L35
Kauffmann J., Pillai T., Zhang Q., Menten K. M., Goldsmith P. F., Lu X., Guzmán A. E., 2017, A&A, 603, A89
Kent S. M., 1994, Ap&SS, 217, 27
Koda J., Sawada T., Hasegawa T., Scoville N. Z., 2006, ApJ, 638, 191
Krumholz M. R., Dekel A., 2010, MNRAS, 406, 112
Kutner M. L., Leung C. M., 1985, ApJ, 291, 188
Larson R. B., 1981, MNRAS, 194, 809
Lequeux J., 2005, The Interstellar Medium
Leroy A. K. et al., 2015, ApJ, 801, 25
Li Q., Tan J. C., Christie D., Bisbas T. G., Wu B., 2018, PASJ, 70, S56
Liu L., Bureau M., Blitz L., Davis T. A., Onishi K., Smith M., North E., Iguchi S., 2021, MNRAS, 505, 4048
Liu L. et al., 2022, MNRAS, 517, 632
Lombardi M., Alves J., Lada C. J., 2010, A&A, 519, L7
Misugi Y., Inutsuka S.-i., Arzoumanian D., 2019, ApJ, 881, 11
Miville-Deschenes M. A., Murray N., Lee E. J., 2017a, VizieR Online Data Catalog, p. J/ApJ/834/57
Miville-Deschênes M.-A., Murray N., Lee E. J., 2017b, ApJ, 834, 57
Miyazaki A., Tsuboi M., 2000, ApJ, 536, 357
Muller E. et al., 2010, ApJ, 712, 1248
Oka T., Hasegawa T., Sato F., Tsuboi M., Miyazaki A., Sugimoto M., 2001, ApJ, 562, 348
Phillips J. P., 1999, A&AS, 134, 241
Pirogov L., Zinchenko I., Caselli P., Johansson L. E. B., Myers P. C., 2003, A&A, 405, 639
Raghuvanshi S., Dutta J., 2022, ApJ, 944, 76
Ramírez-Galeano L., Ballesteros-Paredes J., Smith R. J., Camacho V., Zamora-Avilés M., 2022, MNRAS, 515, 2822
Rebolledo D., Wong T., Xue R., Leroy A., Koda J., Donovan Meyer J., 2015, ApJ, 808, 99
Rice T. S., Goodman A. A., Bergin E. A., Beaumont C., Dame T. M., 2016, ApJ, 822, 52
Rosolowsky E., 2005, PASP, 117, 1403
Rosolowsky E., 2007, ApJ, 654, 240
Rosolowsky E., Blitz L., 2005, ApJ, 623, 826
Rosolowsky E., Leroy A., 2006, PASP, 118, 590
Rosolowsky E., Engargiola G., Plambeck R., Blitz L., 2003, ApJ, 599, 258
Rosolowsky E., Keto E., Matsushita S., Willner S. P., 2007, ApJ, 661, 830
Schruba A. et al., 2017, ApJ, 835, 278
Sodroski T. J. et al., 1995, ApJ, 452, 262
Solomon P. M., Rivolo A. R., Barrett J., Yahil A., 1987, ApJ, 319, 730
Sorce J. G., Tully R. B., Courtois H. M., Jarrett T. H., Neill J. D., Shaya E. J., 2014, MNRAS, 444, 527
Springob C. M. et al., 2014, MNRAS, 445, 2677
Stark A. A., Blitz L., 1978, ApJ, 225, L15
Strong A. W., Mattox J. R., 1996, A&A, 308, L21
Sun J. et al., 2018, ApJ, 860, 172
Tan J. C., 2000, ApJ, 536, 173
Tasker E. J., Tan J. C., 2009, ApJ, 700, 358
Tatematsu K., Ohashi S., Sanhueza P., Nguyen Luong Q., Umemoto T., Mizuno N., 2016, PASJ, 68, 24
Tosaki T. et al., 2017, PASJ, 69, 18
Tully R. B. et al., 2013, AJ, 146, 86
Tully R. B., Courtois H. M., Sorce J. G., 2016, AJ, 152, 50
Utomo D., Blitz L., Davis T., Rosolowsky E., Bureau M., Cappellari M., Sarzi M., 2015, ApJ, 803, 16
Vaceli M. S., Viegas S. M., Gruenwald R., de Souza R. E., 1997, AJ, 114, 1345
van den Bosch R. C. E., Greene J. E., Braatz J. A., Constantin A., Kuo C.-Y., 2016, ApJ, 819, 11
van der Walt S. et al., 2014, PeerJ, 2, e453
Vega Beltrán J. C., Pizzella A., Corsini E. M., Funes J. G., Zeilinger W. W., Beckman J. E., Bertola F., 2001, A&A, 374, 394
Veron-Cetty M. P., Veron P., 1986, A&AS, 66, 335
Williamson D. J., Thacker R. J., Wurster J., Gibson B. K., 2014, MNRAS, 442, 3674
Willick J. A., Courteau S., Faber S. M., Burstein D., Dekel A., Strauss M. A., 1997, ApJS, 109, 333
Wong T. et al., 2011, ApJS, 197, 16
Wong T. et al., 2019, ApJ, 885, 50

## SUPPORTING INFORMATION

Supplementary data are available at *MNRAS* online.

**Table 1.** NGC 5064 cloud properties.

Please note: Oxford University Press is not responsible for the content or functionality of any supporting materials supplied by the authors. Any queries (other than missing material) should be directed to the corresponding author for the article.

This paper has been typeset from a TEX/LATEX file prepared by the author.